Electrochimica Acta 431 (2022) 141154

Contents lists available at ScienceDirect

Electrochimica Acta

journal homepage: www.journals.elsevier.com/electrochimica-acta

Corrosion inhibition of copper and aluminium by 2-mercaptobenzimidazole and octylphosphonic acid—Surface pre-treatment and method of film preparation

Dževad K. Kozlica [a,b], Ingrid Milošev [a,*]

[a] Jožef Stefan Institute, Department of Physical and Organic Chemistry, SI-1000 Ljubljana, Slovenia
[b] Jožef Stefan International Postgraduate School, SI-1000 Ljubljana, Slovenia

A B S T R A C T

The optimal surface pre-treatment conditions for improved adsorption of 2-mercaptobenzimidazole (MBI) and octylphosphonic acid (OPA) on copper and aluminium substrates are presented. For this purpose, mechanical and chemical pre-treatments were employed, which included grinding/polishing and etching/desmutting, respectively. In addition, organic films for both pre-treated samples were prepared by liquid-phase deposition from ethanol or an aqueous solution containing MBI and OPA inhibitors. The mechanism of formation and degradation of the films on Cu and Al samples in 3 wt.% NaCl were investigated by electrochemical methods, whereas morphology and bonding of inhibitors were studied by scanning electron microscopy coupled with energy-dispersive X-ray spectroscopy and X-ray photoelectron spectroscopy. It was shown that the surface pre-treatment did not significantly influence the chemistries of Cu and Al. However, the method of film formation, including the use of two different solvents, was crucial. The inhibitor films on Cu and Al were not formed in an ethanol solution but only deposited from aqueous solutions. A significant reduction in corrosion current density revealed that MBI is an effective inhibitor for Cu, while this characteristic is absent for Al. On the other hand, OPA behaves the other way around.

1. Introduction

The lightweight aluminium alloy (AA) 2024-T3 and other AAs containing Cu are paramount in the aerospace industry due to their high strength-to-weight ratio. However, the heterogeneous nature of the surface microstructure, which consists of alloying elements such as Cu, Mg, Fe, Mn, etc., decreases the alloy's intrinsic corrosion resistance and makes it susceptible to localised corrosion, especially in chloride (Cl^-) containing aqueous solutions. The corrosion initiation was reported to be mainly related to the electrochemical activity of Cu-containing intermetallic particles (IMPs), such as S-phase (Al_2CuMg), θ-phase (Al_2Cu), Al_7Cu_2Fe(Mn) and the surrounding Al matrix [1–5].

To better understand the corrosion processes occurring at IMPs, it would be relevant to monitor the changes that appear on individual metals, aluminium and copper, being the main constituents of AA2024. For this reason, different strategies for replacing carcinogenic chromates have been investigated on aluminium and copper substrates, including environmentally acceptable compounds such as organic inhibitors [6,7]. These organic molecules possess functional group(s) with heteroatom(s) (N, S, P and O) containing lone pair of electrons and/or delocalised π electrons due to the presence of multiple bonds or aromatic rings [8,9], thus enabling chemical adsorption onto metal surfaces.

Azole molecules and their derivatives are some common effective organic inhibitors that are often used to protect copper [10–15]. Benzotriazole (BTA) has been widely known and used in industry due to its unsurpassed efficiency [16]. However, Žerjav and Milošev showed that BTA is an inefficient inhibitor under acidic conditions (pH = 5) [17]. In the past few decades, 2-mercaptobenzimidazole (MBI) has been established as a promising candidate for copper protection that provides a high level of inhibition not only in near-neutral chloride solutions [10,13,15,18–20], but also in acidic conditions (below pH 5) [21]. The high corrosion inhibition efficiency of MBI for copper in 3 wt.% NaCl aqueous solution and its bonding mechanism were reported by Finšgar [13,19] and Milošev et al. [10,15], where MBI acts as a mixed type (anodic and cathodic) inhibitor with a stronger anodic effect. In addition, our group recently reported that MBI in binary combination with octylphosphonic acid (OPA) synergistically boost corrosion inhibition of copper [21]. Chiter et al. [22] showed that MBI also has the ability to enhance the barrier properties of de-passivated or incompletely passivated copper surfaces by healing the damaged oxide surface. Izquierdo et al. investigated metal−inhibitor interactions using localised scanning micro-electrochemical techniques. They revealed that MBI forms thicker and more insulating organic films on copper in sodium chloride solution than in neutral sodium sulfate solution [23], which is most likely

* Corresponding author.
E-mail address: ingrid.milosev@ijs.si (I. Milošev).

https://doi.org/10.1016/j.electacta.2022.141154
Received 10 July 2022; Received in revised form 1 September 2022; Accepted 5 September 2022
Available online 6 September 2022

attributed to the involvement of Cl^- ions in the formation of Cu-MBI inhibitory film. Our recent paper confirmed this effect by a detailed XPS and ToF-SIMS investigation [24]. Results showed that the chloride ions act simultaneously as a promoter and a reactant, thus revealing their dual role in forming polymerised Cu-Cl-MBI chains.

Other compounds, such as alkylphosphonic acids [25–30] have been used to form well-ordered self-assembled monolayers (SAMs) on oxide-covered metal surfaces. Such SAMs increase hydrophobicity [31] of metal surfaces and exhibit the advantages of high coverage, few defects, and high inhibition efficiency [32,33]. Phosphonic acids increase the hydrophobicity of metal surfaces and offer high inhibition efficiency. They have been used due to their stability and ability to form complexes with metal cations. Maege et al. [34] reported that adsorbed octadecylphosphonic acid (ODPA) on an aluminium substrate formed orientated layers proved by polarised external reflectance FTIR measurements. Schwartz's group established the growth of an ODPA monolayer on mica as a model system where atomic force microscopy (AFM) observations showed that growth proceeded via nucleation, growth, coalescence, etc., of densely packed molecular aggregates (islands) [35–37]. Furthermore, they showed that ODPA could form dense SAMs on the sapphire (corundum) surface, which have a good inhibition effect on overall corrosion [38]. Hoque et al. [25] reported denser packing and better orientation of the alkylphosphonic acid molecules with longer chain lengths on copper oxide surfaces. A quantum chemical density functional theory (DFT) investigation has provided insight at the atomic level regarding the molecular adsorption probabilities and corresponding bonding energies of six different anchor groups (carboxylic, benzoic, amino, imidazole, phosphonic and thiol) on hydroxylated oxidised aluminium surfaces and showed that among these anchor groups phosphonic groups adsorb the strongest. In contrast, thiol group does not adsorb [30].

The main point of interest in this work is the influence of surface pre-treatment before applying corrosion inhibitors. Surface pre-treatments of metal surfaces, either mechanical and/or chemical, usually target improved bonding ability with inhibitor molecules, conversion coatings, primers or paints and increased corrosion resistance in corrosive environments [39–44]. The mechanical pre-treatment, including grinding and/or polishing, is usually based on SiC sandpaper and produces a macro-rough surface [45,46]. The chemical pre-treatment typically involves several steps: (i) degreasing, (ii) etching and (iii) desmutting. Effective cleaning produces a contaminant-free surface. The main surface contaminants that require removal with degreasers (acetone) come from the processing and shaping of metals and alloys (lubrication oils). Alkaline etching, usually performed using sodium hydroxide, generates complex oxides and hydroxides of aluminium, and removes any organic residue and several micrometres of the metal/alloy. Some of these reaction products, including intermetallic compounds, are insoluble in the etch solution. These remain on the surface of the aluminium parts in the form of "smut". The etching step is followed by applying acid deoxidiser (also called desmutting or pickling), such as nitric acid, to remove any residue, i.e., dissolve the surface oxide or smut, from – or caused by – the previous alkaline step [40,46]. The studies showed that the aluminium (hydr)oxides with large amounts of active surface sites (high surface area and low-crystalline) are more active than the well-crystalline (hydr)oxides with lower surface area [31,39]. Abd-El-Naby et al. reported that the lupine extract is more effective as an inhibitor for non-etched than the etched aluminium [42]. The adsorption of carboxylic acids and, consequently, the effect on corrosion protection was more efficient on the acid-etched copper surface [47] than on the ground surface. Similar behaviour was observed for alkaline-etched aluminium, where the adsorption of carboxylic acids and other organic inhibitors required a micrometre-level rough surface [31]. On the ground Al surface, the adsorption was unsuccessful.

Herein we report the influence of surface pre-treatment of Al and Cu on the adsorption of MBI and OPA on the metal substrates. In addition, a different method of preparation to facilitate the adsorption of inhibitors was also examined. To this end, organic layers were prepared by simple liquid-phase depositions, i.e., by immersion of individual Al and Cu samples either directly in chloride-containing inhibitor aqueous solution or prepared by immersion in a non-aqueous inhibitor solution [17,31,48]. The corrosion inhibition effectiveness was investigated utilising potentiodynamic polarisation curves, whereas cyclic voltammetry (CV) was employed to study the film formation and degradation processes on the metal substrate. In addition, the surface characterisation of the pre-treated surfaces before and after formed films was performed by X-ray photoelectron spectroscopy (XPS) and scanning electron microscopy combined with energy-dispersive X-ray spectroscopy (SEM-EDS).

2. Experimental

2.1. Materials, substrate preparation and chemicals

Working electrodes were prepared from a 2 mm thick copper and aluminium sheet (Goodfellow, Cambridge, UK, purity of 99.9% and 99.0%, respectively) and cut out in the form of discs 15 mm in diameter.

The surface of the samples was either mechanically or chemically pre-treated. First, using a rotating plate polisher, the samples were successively water-ground with P1000 and P2400-grit SiC emery papers (provided by Struers, Ballerup, Denmark), followed by polishing with a polish nap (MD, Mol, Struers, Ballerup, Denmark) using water diamond suspension up to 3 μm (DiaDuo, Struers, Ballerup, Denmark) to obtain a uniform, mirror-like surface appearance. These samples were denoted as mechanically (mc) pre-treated. Then, another set of aluminium and copper samples was chemically (ch) pre-treated, i.e., aluminium was etched in 0.01 M NaOH for 10 min at 60 °C followed by desmutting in 10% HNO_3 for 3 min at room temperature, while copper was slightly etched in 10% HNO_3 for 3 min at room temperature. After any pre-treatment, the surfaces were subject to ultrasonic cleaning in absolute ethanol (Panreac AppliChem, Germany, purity of 99.8%) for 3 min, double-rinsed with Mili-Q water (Millipore, Billerica, MA, USA, resistivity 18.2 MΩ cm at 25 °C) and blown dry with nitrogen gas.

The chemicals utilised for Cu and Al modification were sodium chloride (NaCl, purity 99.5%, supplied by Fisher Scientific), 2-mercaptobenzimidazole (MBI, purity 98%, supplied by Sigma Aldrich) and octylphosphonic acid (OPA, purity of 98%, supplied by Ark Pharm, Inc.). All the reagents were used as received without further modification.

2.2. Preparation of organic films

Organic films for both types of pre-treated samples were prepared by liquid-phase deposition either from ethanol (et) or aqueous (aq) solution containing MBI (S) and OPA (P).

1 Liquid-phase deposition from EtOH inhibitor solution: Mechanically or chemically pre-treated copper and aluminium samples were immersed for 30 min in an ethanol medium at a concentration of 1 mM. After immersion, samples were rinsed with water, dried in the stream of nitrogen and then subject to electrochemical and surface characterisation. Electrochemical measurements were conducted in 3 wt.% NaCl solution.
2 Liquid-phase deposition from aqueous NaCl + inhibitor solution: Mechanically or chemically pre-treated copper and aluminium samples were immersed for 24 h in an aqueous aggressive chloride medium (i.e. 3 wt.% NaCl) with the addition of individual MBI or OPA organic compounds at a concentration of 1 mM. After denoted immersion period (24 h), the samples were removed from the solution, double rinsed gently with deionised water, dried in the stream of nitrogen and then subject to electrochemical and surface characterisation. Electrochemical measurements were conducted in 3 wt.% NaCl solution containing 1 mM inhibitor MBI or OPA.

The same surface pre-treatments were used for both Cu and Al

(mechanical and chemical) and the same preparation methods (ethanolic and NaCl aqueous and solutions). The time of immersion, however, differed: it was 30 min in the former and 24 h min in the latter. Although the inhibition effect in NaCl was already evident after 30 min, the immersion was prolonged to get relevant results on the stability of the formed layer for 24 h. In contrast, the prolongation of immersion in ethanolic solution was not of interest since this method was meant as a fast pre-preparation of the layer. Our previous study [30] showed that prolonging immersion time did not significantly contribute to more efficient layer formation.

All the utilised solutions and their as-prepared pH and shorthand labels are summarised in Table S1. The pH values of the solutions used for immersion of Cu and Al samples were not adjusted to match that of NaCl but were used as-prepared. The pH values of solutions used for surface modification of Al samples were adjusted to 7 since aluminium undergoes dissolution in aqueous solutions below pH 4.

2.3. Electrochemical measurements

Electrochemical measurements were carried out in an open-to-air conventional three-electrode cell assembly using PGSTAT M204 Autolab (Metrohm Autolab, Utrecht, Netherlands) multichannel potentiostat/galvanostat controlled by NOVA software. The working electrodes (WE) were copper and aluminium discs pressed against a Teflon O-ring with a 1 cm^2 exposed surface area. A Pt mesh and an Ag/AgCl/$KCl_{sat'd.}$ (0.197 V vs. standard hydrogen electrode) were employed as the counter electrode and the reference electrode, respectively. The latter was used with a Luggin capillary to minimise IR drops at the WE surface. In the text, potentials are given with respect to Ag/AgCl/$KCl_{sat'd.}$ electrode.

Once the measurement started, specimens were allowed to rest for approximately 1 h until a near steady-state of open circuit potential (OCP), denoted as E_{OCP}, was established. A steady state is assumed to be reached when the E_{OCP} changes less than 5 mV over 10 min [49]. Electrochemical measurements for organic films prepared by aqueous-phase deposition were carried out in NaCl solution containing inhibitor, except the blank solution contained only 3 wt.% NaCl. In contrast, measurements for the films obtained by ethanol-phase deposition were performed only in NaCl solution. Reported results were based on at least three experiments to ensure reproducibility. Measurements were carried out at ambient temperature (23 °C). Representative curves were chosen to be presented in the figures. In tables, values for E_{corr} and j_{corr} are given as mean ± standard deviation.

2.3.1. Potentiodynamic polarisation curves

Through the DC polarisation technique, information on the corrosion rate, pitting susceptibility, passivity, and cathodic behaviour of an electrochemical system may be obtained [50]. The potentiodynamic polarisation curves were recorded starting in the cathodic range 250 mV below E_{OCP} and increasing the potential in the anodic direction up to 1 V at a scan rate of 1 mV s^{-1}.

The application of the mixed potential theory allows the determination of the corrosion rate using the Tafel extrapolation method. Due to the contribution of the back reaction to the forward reaction at lower overpotentials, extrapolation of the linear portions of the polarisation curve was performed at potentials well away from the corrosion potential (E_{corr}), i.e. in the range of 60 to 120 mV [51]. The corrosion current density (j_{corr}) was estimated from the intersection of the anodic and cathodic Tafel slopes at E_{corr}. It should be emphasised that some polarisation curves with not well-defined anodic Tafel region were extrapolated by inspecting only a linear fit of the cathodic Tafel curve, which intersects E_{corr}.

2.3.2. Cyclic voltammetry

The cyclic voltammograms were recorded through a linear potential sweep in the potential range from −0.6 V to 1 V with a scan rate of 1 mV s^{-1}. Gaussian peak function was used for fitting the cyclic voltammogram. To access the adsorption mechanisms, one set of experiments included measurements with different scan rates, i.e., 1, 5 and 10 mV s^{-1}. The results are based on at least three experiments to ensure reproducibility.

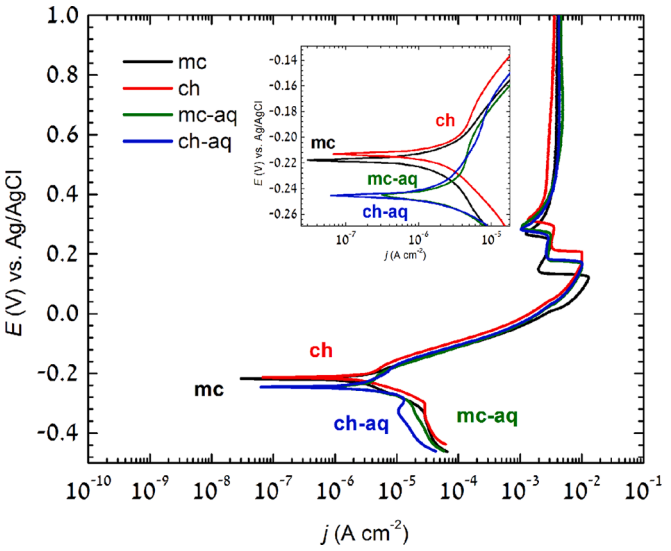

Fig. 1. Potentiodynamic polarisation curves recorded for copper samples in 3 wt.% NaCl solution. The copper surface before measurements implies mechanical pre-treatment and chemical pre-treatment. The difference between mc (ch) and mc-aq (ch-aq) samples is only immersion time; the former was immersed for 1 h and the latter for 24 h in chloride solution. The area around E_{corr} is shown at the enlarged scale in the inset.

2.4. Surface characterisation

2.4.1. X-ray photoelectron spectroscopy

X-ray photoelectron spectroscopy (XPS) was used to determine the presence of the oxide and organic layers and the elemental composition in the first few nanometres of a surface [26]. XPS analysis was performed on a TFA Physical Electronics Inc. spectrometer equipped with a hemispherical analyser. All the spectra were acquired utilising a monochromatic Al Kα X-ray source (1486.6 eV) with an analysed area of 400 μm. Survey scan spectra were obtained at a pass energy of 187.9 eV, while the core level single peaks were measured at pass energy of 29.4 eV with an energy step of 0.1 eV. The take-off angle, defined as the emission angle normal to a sample surface, was 45° The binding energies (E_b) were calibrated by reference to the C 1 s photoelectron peak at 284.8 eV. The uncertainty in the binding energy scale is estimated to be 0.2 eV. The linear method was used for the Cu 2p line and the iterative Shirley method for the Cu LMM, followed by smoothing using a Savitzky-Golay algorithm [52]. The quantitative analysis of the species at the surface was derived from the peak area intensities. Quantification was carried out using the MultiPak processing software. The estimated relative error for all XPS data used for elemental quantification is ± 2%.

2.4.2. Scanning electron microscopy coupled with energy-dispersive X-ray spectroscopy

Scanning electron microscopy combined with energy-dispersive X-ray spectroscopy (SEM-EDS) was applied to reveal the morphology and semi-quantitative composition of the surface at areas of interest, with an analysis depth of about 1 μm. SEM images were recorded in secondary electron (SE) and back-scattered electron (BSE) imaging modes at beam energies of 5 keV and 15 keV, respectively, using a field emission (FE) SEM JSM 7600F, JEOL, Japan, equipped with EDS (Inca Oxford 350 EDS SDD). Before analysis, Al and Cu samples were coated with a thin carbon layer to reduce the charging effect.

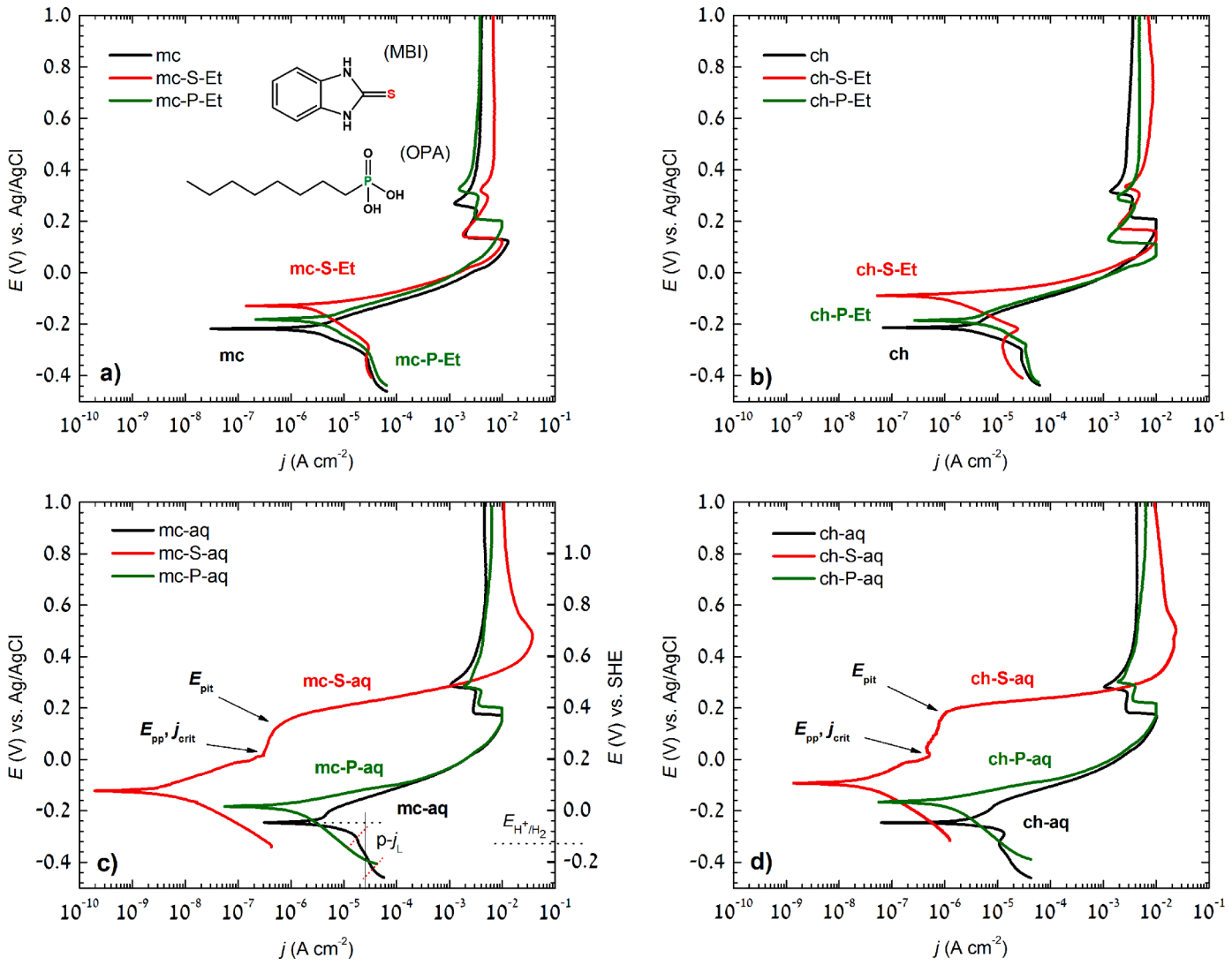

Fig. 2. Potentiodynamic polarisation curves recorded for copper in (a and b) 3 wt.% NaCl solution and (c and d) 3 wt.% NaCl with the addition of 1 mM OPA or MBI. The copper surface before measurements implies: (a) mechanical pre-treatment + deposition of inhibitors from ethanol solution, (b) chemical pre-treatment + deposition from ethanol solution, (c) mechanical pre-treatment + deposition from aqueous solution, and (d) chemical pre-treatment + deposition from aqueous solution.

3. Results and discussion

3.1. Copper

3.1.1. Potentiodynamic polarisation curves

Fig. 1 shows the potentiodynamic polarisation curves for mechanically (mc) and chemically (ch) pre-treated copper samples without inhibitor (i.e., control samples) in 3 wt.% NaCl solution open to the air. Utilising the Pourbaix (E vs. pH) diagram of copper in chloride-containing aqueous solution [53], it can be assumed that at the mean E_{corr} (−250 mV) and more positive potentials (to approximately 1000 mV), Cu reacts to form chloride species such as CuCl and $CuCl_2^-$, and Cu^{2+} ions. It is generally accepted that the anodic dissolution of copper in neutral NaCl solutions is a mass transfer rather than an activation controlled process in which the diffusion of soluble $CuCl_2^-$ species from copper to the bulk of the solution is the rate-determining step [53–55]. As long as the salt film is present, the dissolution process is governed by diffusion kinetics [56].

The related anodic polarisation curve recorded for the control sample (mc) after 1 h at OCP demonstrates apparent Tafel behaviour with a slope of 61 mV/dec, which corresponds to 2.3 RT/F, i.e., 59 mV/dec (Fig. 1) [53,54]. In addition, it should be noted that the ch curve shows similar electrochemical characteristics as mc.

Considering the potentiodynamic polarisation response of Cu measured after 24 h immersion in chloride solution (mc-aq), a small passivity at lower overpotentials was noticed that is barely observed for mc (Fig. 1). This makes determining the anodic Tafel slope difficult. It is more appropriate to determine it from the cathodic branch and intersection with E_{corr} (Fig. 2c). The mc-aq sample was immersed in chloride solution for 24 h at OCP before the polarisation measurements. In comparison, mc was immersed for 1 h at OCP before the potentiodynamic polarisation testing in 3 wt.% NaCl. Prolonged exposure to NaCl solution may indicate a thicker barrier layer of Cu_2O on the porous and poorly protective CuCl layer [54,57,58]. The layer formed during prolonged immersion results in the appearance of the narrow passivation region due to the existence of a CuCl/Cu_2O film. The abrupt increase of the current density at the corresponding pitting potential (E_{pit}) may suggest the occurrence of pitting corrosion [58]. The pitting behaviour is caused by the ease of penetration of chloride ions at some insufficiently protected sites on the surface of Cu, which are weak spots where the localised attack begins.

Although anodic behaviour is the area of primary interest, it is

necessary to note a few observations regarding cathodic polarisation behaviour. The only oxidants (i.e., reducible species) in near-neutral chloride solutions open to the air (pH = 5.5) were dissolved oxygen and hydrogen ions. Examination of the cathodic polarisation curve for mc-aq (Fig. 2c) shows that the E_{corr} is higher than the equilibrium potential of H^+/H_2, i.e., $E_{H^+/H_2} = -0.0591$ (pH) vs. V_{SHE} at 25 °C ($2H^+ + 2e^- \longrightarrow H_2$); therefore, at potentials immediately below the E_{corr}, cathodic behaviour is governed by the oxygen reduction reaction (ORR) [53]. In practice, the limit of $2H^+ + 2e^- \longrightarrow H_2$ has been moved towards more negative values because the cathodic polarisation, initiated 250 mV below the E_{corr} and then gradually increased towards more positive values, caused the rise of pH in local regions. If the solution is stationary and/or when the pH is higher in the presence of dissolved O_2, diffusion of H^+ ions will be slow, and concentration polarisation can shorten the linear Tafel region in the cathodic branch. For a scenario like the mc-aq case, linearity disappears altogether, with the cathodic reaction now under combined activation and diffusion control at E_{corr}; the contribution of mass transport is predominant based on the high cathodic slope [53,59]. Also, at higher cathodic overpotentials (i.e., at lower potentials, near the region of polarisation initiation), the activation polarisation and concentration polarisation co-occur; the O_2 reduction is under diffusion control, and the H^+ reduction is under activation control [51]. All the results taken together lead to the conclusion that at E_{corr}, the ORR is under mixed kinetic control.

Another interesting feature is that at a potential of −0.33 V, a cathodic current peak was observed (especially for the ch-aq), which may be attributed to the reduction of Cu_2O film. The surface composition of the ch-aq (Table 3) revealed the presence of Cu_2O, so it is reasonable to expect its reduction during cathodic polarisation. This conclusion is consistent with the results of Benzbiria et al. [59], obtained by rotating disk electrode (RDE), where the cathodic peak at −0.29 V independent of the electrode rotation rate was reported. Given that anodic and cathodic curves (mc-aq and ch-aq) do not show a clear Tafel region, we suggest that the most appropriate procedure to determine the corrosion current of the system would be the extrapolation of the cathodic pseudo-limited-current density (p-j_L) back to the zero overvoltage (Fig. 2c and d). The term „pseudo“ was introduced to denote a deviation from the conditions of pure mass transfer. The p-j_L was determined as the halfway point of the potential limits of the linear cathodic region and was estimated to be 25 μA cm^{-2} under stagnant electrolyte conditions, which is close to the literature value of 20–30 μA cm^{-2} in neutral solution, as reported by Vukmirovic et al. [60] using RDE set-up. The more accurate j_L or the contribution of charge transfer could be derived from the Koutecky-Levich equation [61] in the RDE measurements. Because the net rate of the anodic reaction (i.e., copper corrosion) must equal the net rate of the cathodic reaction (i.e., mainly oxygen reduction), and given that the slowest reaction controls the rate of corrosion, it can be concluded that ORR kinetics determine the general corrosion rate of copper at the OCP because the ORR is slower than the anodic dissolution of copper [49,51]. Since the corrosion of copper is under cathodic control (predominantly controlled by concentration polarisation), it is, therefore, crucial for reducing the rate of ORR.

Organic films for both types of pre-treated samples were prepared by liquid-phase deposition either from ethanol (et) or aqueous (aq) solution containing MBI (S) and OPA (P) inhibitors. The current density responses of the mc-S-Et and mc-P-Et (Fig. 2a), but also the ch-S-Et and ch-P-Et (Fig. 2b), seem to be very similar to the control sample mc and ch. The only difference is that the OCP of both samples modified with MBI, S-mc-Et and S-ch-Et, is shifted towards more positive values for ca. 40 mV. This could mean that the possibly pre-formed Cu-MBI layer in ethanol immediately falls off the electrode when immersed in NaCl solution. Moreover, the chemical composition (see below, Table 3) of the copper surface, derived from the XPS spectra, revealed the absence of sulphur and phosphorus, indicating that neither Cu-MBI nor Cu-OPA films were present after the functionalisation step in the ethanolic solution of MBI and OPA followed by immersion in NaCl solution for 24 h, respectively (see below).

Table 1
Electrochemical parameters – corrosion potential (E_{corr}), corrosion current density (j_{corr}), pitting potential (E_{pit}), passive range ($\Delta E_{pass} = |E_{pit} - E_{corr}|$), passive current density (j_{pass}), anodic Tafel slope (b_a) and cathodic Tafel slope (b_c) deduced for Cu from the potentiodynamic polarisation curves (Figs. 1 and 2). Values for E_{corr} and j_{corr} are given as mean ± standard deviation.

Cu samples	E_{corr} (mV)	j_{corr} (A cm^{-2})	E_{pit} (mV)	ΔE_{pass} (mV)	j_{pass} (A cm^{-2})	b_a (mV/dec)	$-b_c$ (mV/dec)
mc-aq	−243 ± 6	(2.22 ± 0.10) × 10^{-5}	−200	50	4.67 × 10^{-6}	64	384
mc-S-aq	−133 ± 10	(6.12 ± 0.93) × 10^{-9}	160	280	3.86 × 10^{-7}	74	103
mc-P-aq	−165 ± 5	(2.23 ± 0.08) × 10^{-6}	–	–	–	48	204
ch-aq	−233 ± 29	(1.70 ± 0.32) × 10^{-5}	−172	70	8.98 × 10^{-6}	61	295
ch-S-aq	−94 ± 4	(2.36 ± 0.84) × 10^{-8}	200	290	6.50 × 10^{-7}	105	120
ch-P-aq	−174 ± 17	(1.68 ± 0.62) × 10^{-6}	–	–	–	31	164

In contrast to the inhibitor deposition from the ethanol solution, mechanically (S-mc-aq) and chemically (S-ch-aq) pre-treated copper specimens were prepared by 24 h immersion in aqueous NaCl+MBI, followed by potentiodynamic measurements in NaCl+MBI solution.

For such prepared specimens, the current densities of both corrosion reactions are diminished together with the shift of E_{corr} more positive than the control sample (mc-aq) (Fig. 2c and d). This can be attributed to the Cu(I) complexation with MBI and subsequent adsorption of the complex formed on the copper surface. Because there is a significant reduction in the j_{corr} by almost four orders of magnitude, MBI is considered a very effective corrosion inhibitor for copper in an aqueous chloride-containing solution. In the Tafel region, only a small portion of the anodic Tafel slope is available, which is considered not well-defined. The linearity between E and log j is interrupted after the primary passivation potential, E_{pp}, is reached, whereby significant passivity occurs. The improved resistance to localised corrosion is reflected by increased pitting (breakdown) potential, as shown in the polarisation curves of Fig. 2c.

Regarding the cathodic polarisation curve for mc-S-aq, an evident change in kinetics relative to the control sample was observed. The Tafel region with a corresponding slope of approx. 100 mV/dec was established with a significant decrease in current density, indicating a charge-transfer controlled process, i.e., the rate of oxygen reduction is controlled by the potential across the interface, not by the rate at which dissolved oxygen diffuses to the metal surface. It is believed that the adsorption of MBI molecules on the surface of copper minimises the number of active sites where oxygen is expected to adsorb.

The same is true for the ch-S-aq. The anodic current density increases as an exponential function of potential until reaching a critical passivating current density, j_{crit}, at E_{pp}, at which point a large decrease in current density is observed in an upward scan (Fig. 2d). Moreover, ch-S-aq shows somewhat more positive E_{corr} and broader ΔE_{pass}, but larger j_{corr} by a factor of 5 with respect to mc-S-aq. It is difficult to decide which of these two samples has an advantage in corrosion protection because their electrochemical parameters are comparable (Table 1). In summary, the polarisation curves in Fig. 2c and d (red curves) showed that MBI is a mixed-type inhibitor for copper in aqueous chloride solutions. It reduces the rate of the anodic reaction more strongly than the cathodic reaction rate and makes the OCP of copper more positive. Unlike MBI, the OPA

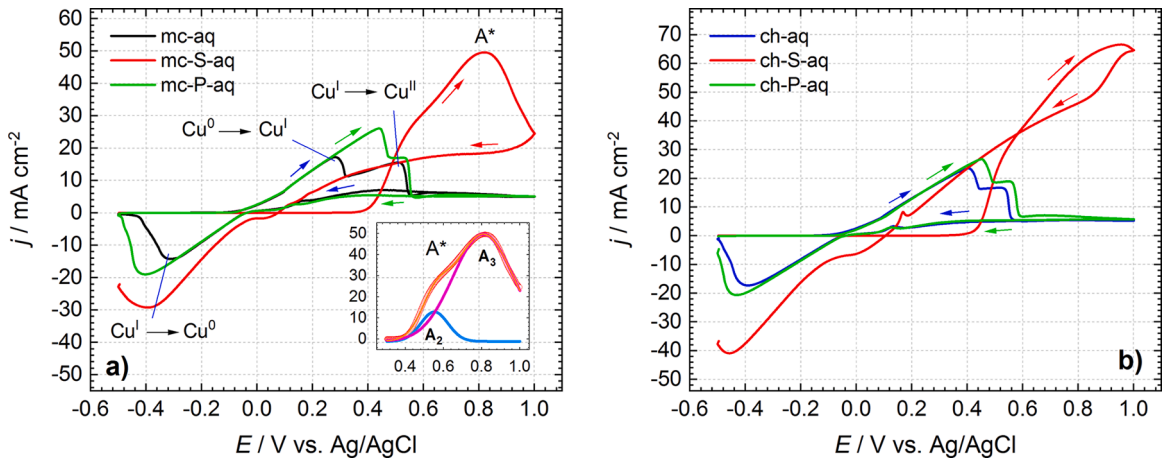

Fig. 3. Cyclic voltammograms recorded for copper in 3 wt.% NaCl solution with and without the addition of 1 mM OPA or MBI at a scan rate of 10 mV s^{-1}. The copper surface before measurements implies: (a) mechanical pre-treatment + deposition of inhibitors from aqueous solution and (b) chemical pre-treatment + deposition of inhibitors from aqueous solution.

induces only a slight reduction of charge transfer on Cu (Fig. 2c and d). Interestingly, the contribution of mass transfer for the cathodic reaction is significantly smaller than the control sample.

Moreover, the j_{corr} for mc-P-aq is smaller than for mc-aq by 5 times, but without any significant impact since pitting occurs immediately (i.e., at the OCP). Generally, at E_{pit}, the current density rises due to the active dissolution within developing corrosion pits. The same is true for the ch-P-aq relative to the control ch-aq Cu sample. Inferior inhibitory properties of OPA have been confirmed by the absence of phosphorus content on the copper surface for both samples, mc-P-aq and ch-P-aq (Table 3).

3.1.2. *Cyclic voltammetry*

Fig. 3 shows cyclic voltammograms for copper-based samples: mc-aq, mc-S-aq, mc-P-aq, ch-aq, ch-S-aq and ch-P-aq, recorded in 3 wt.% NaCl solution with and without added MBI and OPA inhibitors after 24 h of immersion at a scan rate of 10 mV s^{-1}. For mechanically pre-treated copper sample immersed in 3 wt.% NaCl solution (mc-aq), two anodic peaks at 0.29 V (peak A_1) and 0.52 V (peak A_2) in the forward scan, and a single cathodic peak at −0.31 V (peak C_1) in the reverse scan, are observed (Fig. 3a). Peak A_1 can be attributed to the formation of CuCl salt via $Cu + Cl^- \longrightarrow CuCl_{(s)} + e^-$ [53,62]. The shoulder peak A_2 accounts for the electro-oxidation of Cu(I) to soluble Cu^{2+} followed by a limiting current in the plateau region, the equilibrium between CuCl and $CuCl_2^-$ ($CuCl_{(s)} + Cl^- \longrightarrow [CuCl_2]^-$) [11,53,62–64]. The intensity of the limiting current indicates a poorly protective and porous film. The only cathodic peak, C_1, is ascribed to the reduction of Cu(I) to Cu(0), i.e., CuCl to Cu [11,53,62–64].

Chemisorbed MBI on the Cu substrate, mc-S-aq, retard electron transfer across the electrode interface so that the peak A_1 disappears completely, suggesting an excellent inhibition efficiency (Fig. 3a). Such behaviour coincides with the existence of passivation observed in polarisation curves measurements (vide supra, Fig. 2a). The current suddenly rose sharply at potentials above 0.4 V, reaching the maximum at 0.82 V (peak A*). The position of this prominent peak is at more positive potential than expected to be attributed to a simple transition from Cu(I) to Cu(II). We reported previously [24] that the enlarged current densities of the peak A* could be assigned to the film degradation caused by oxidative dimerisation of Cu(I)-MBI according to:

$$2\text{Cu-MBI} \longrightarrow 2Cu^{2+} + (MBI)_2 + 4e^- \quad (1)$$

The overall oxidation reaction consists of the two competing half-cell reactions:

$$2Cu^{+} \longrightarrow 2Cu^{2+} + 2e^- \quad (2)$$

$$2MBI^- \longrightarrow (MBI)_2 + 2e^- \quad (3)$$

It is striking to note that, indeed, the peak A*(inset of Fig. 3a) may be deconvoluted into two Gaussian peaks: (a) the smaller peak labelled A_2, which could be attributed to the anodic oxidation of Cu(I) to Cu (II) ions (Eq. (2)), and (b) a broader and larger peak labelled A_3, which could correspond to the oxidative dimerisation of MBI^- (Eq. (3)). The peak A_2 becomes noticeable at higher sweep rates such as 10 mV s^{-1}. This is why we did not notice it earlier, where all measurements were performed at a scan rate of 1 mV s^{-1} [24]. The interpretation of observed phenomena coincides with the results of XPS and ToF-SIMS investigation of the products collected after cyclic voltammetry run, which is discussed in detail in our recent publication [24].

Using the Gaussian peak function to fit the cyclic voltammogram does not provide information on the actual A_2/A_3 peak ratio but qualitatively shows the components comprising the larger A* peak.

It is noteworthy that the oxidation of Cu(I) to Cu(II) is an irreversible process since the soluble Cu^{2+} species diffuse away from the electrode surface and thus cannot be reduced in the cathodic scan. On the other hand, the transition from Cu(0) to Cu(I) is a partially irreversible system, where the cathodic peak is not as pronounced as the anodic one ($I_{p,a}/I_{p,c} \neq 1$) and the peak-to-peak separation is greater than 59 mV at 25 °C ($\Delta E_p > 0.059$ V). There is a high barrier to electron transfer, i.e. slow electron transfer at the electrode surface, so the more positive (negative) potentials are required to observe oxidation (reduction) reactions, giving rise to larger ΔE_p [65].

The voltammogram in Fig. 3b for the chemically pre-treated copper sample shows similar redox trends as mechanical pre-treatment. However, a few significant differences should be highlighted. First, the intensities of the peaks A_1 and A_2 for ch-aq in chloride solution are greater than for the mc-aq. This can be explained based on the SEM image (see below Fig. 6), which suggests that the chemical treatment caused an increased surface roughness, increasing the surface area and thus, current densities. Second, the $i_{p,a}$ of the A* for ch-S-aq is also higher than the $i_{p,a}$ for the mc-S-aq, indicating that more Cu-MBI film was degraded, which is a simple consequence of an immense amount of adsorbed inhibitor during the process of organic film formation. XPS surface analysis revealed (Fig. 5, Table 3) a higher elemental ratio between N and S for ch-S-aq compared to mc-S-aq (Table 3), which is consistent with a larger surface area caused by chemical etching (Fig. 6).

Another interesting feature of the copper samples protected with MBI (i.e., mc-S-aq and ch-S-aq) is that the cathodic peak C_1 exists in the reverse scan, although the corresponding anodic peak A_1 does not appear at all in the forward scan. This should be no surprise given that Cu-MBI film formation was accompanied by the formation of Cu_2O underlayer during the preparation of samples mc-S-aq and ch-S-aq. Such

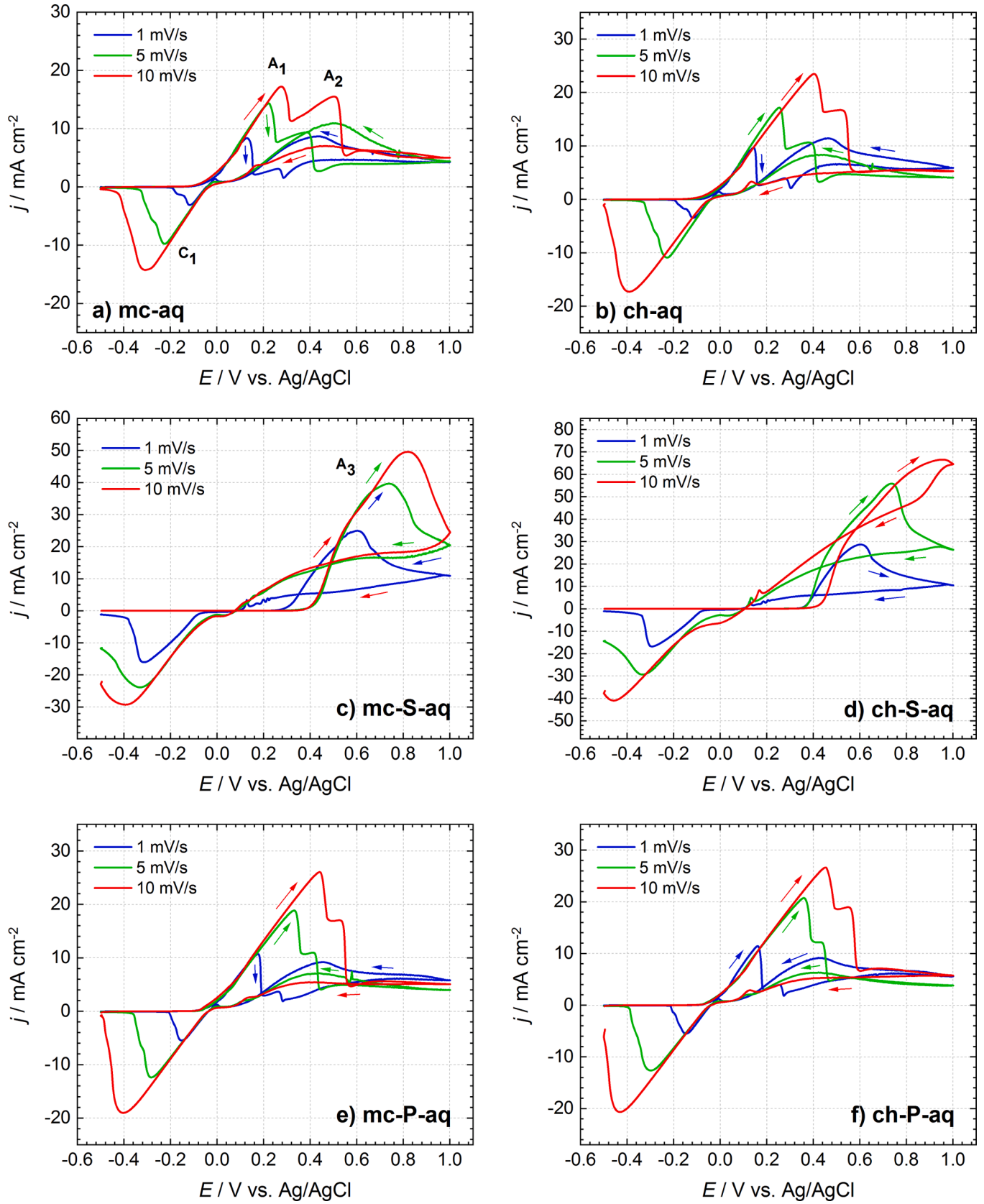

Fig. 4. Cyclic voltammograms recorded for copper in 3 wt.% NaCl solution with and without adding 1 mM OPA or MBI at different scan rates; 1, 5 and 10 mV s^{-1}. The copper surface before measurements implies: (a) mechanical pre-treatment, control sample, (b) chemical pre-treatment, control sample, (c) mechanical pre-treatment + deposition of MBI from aqueous solution, and (d) chemical pre-treatment + deposition of MBI from aqueous solution, (e) mechanical pre-treatment + deposition of OPA from aqueous solution, and (f) chemical pre-treatment + deposition of OPA from aqueous solution.

Table 2
The relationships between the peak current (j_p), peak potential (E_p), and the square root of the scan rate ($\nu^{1/2}$) for redox reactions that obey the passivation model deduced from the cyclic voltammograms for Cu (Fig. 4).

Samples	$j(A_1)$ (mA cm^{-2})	$E(A_1)$ (mV)	$j(A_2)$ (mA cm^{-2})	$E(A_2)$ (mV)
	Passivation model			
	$j_p = x \cdot \nu^{1/2} + y$	$E_p = x' \cdot \nu^{1/2} + y'$	$j_p = x \cdot \nu^{1/2} + y$	$E_p = x' \cdot \nu^{1/2} + y'$
mc-aq	$j_p = 4.18 \cdot \nu^{1/2} + 4.41$ ($R^2 = 0.9889$)	$E_p = 69.56 \cdot \nu^{1/2} + 61.65$ ($R^2 = 0.9989$)	$j_p = 5.70 \cdot \nu^{1/2} - 2.72$ ($R^2 = 0.9946$)	$E_p = 110.68 \cdot \nu^{1/2} + 147.28$ ($R^2 = 0.9988$)
ch-aq	$j_p = 6.41 \cdot \nu^{1/2} + 3.16$ ($R^2 = 0.9986$)	$E_p = 0.12 \cdot \nu^{1/2} + 0.01$ ($R^2 = 0.971$)	$j_p = 5.94 \cdot \nu^{1/2} - 2.23$ ($R^2 = 0.9964$)	$E_p = 0.11 \cdot \nu^{1/2} + 0.15$ ($R^2 = 0.9615$)
mc-S-aq	$j_p = 11.22 \cdot \nu^{1/2} + 13.37$ ($R^2 = 0.9990$)	$E_p = 102.37 \cdot \nu^{1/2} + 501.67$ ($R^2 = 0.9946$)		
ch-S-aq	$j_p = 17.76 \cdot \nu^{1/2} + 12.75$ ($R^2 = 0.9752$)	$E_p = 182.42 \cdot \nu^{1/2} + 360.95$ ($R^2 = 0.9717$)		
mc-P-aq	$j_p = 7.05 \cdot \nu^{1/2} + 3.57$ ($R^2 = 0.9976$)	$E_p = 125.12 \cdot \nu^{1/2} + 46.49$ ($R^2 = 0.9994$)	$j_p = 6.13 \cdot \nu^{1/2} - 2.47$ ($R^2 = 0.9981$)	$E_p = 125.12 \cdot \nu^{1/2} + 136.49$ ($R^2 = 0.9994$)
ch-P-aq	$j_p = 7.11 \cdot \nu^{1/2} + 4.53$ ($R^2 = 0.9960$)	$E_p = 140.00 \cdot \nu^{1/2} + 28.09$ ($R^2 = 0.9885$)	$j_p = 7.01 \cdot \nu^{1/2} - 3.25$ ($R^2 = 0.9886$)	$E_p = 139.55 \cdot \nu^{1/2} + 115.69$ ($R^2 = 0.9951$)

a finding was previously published by our group [24]. When such a sample is anodically polarised, the A_1 peak, corresponding to the oxidation of Cu(0) to Cu(I), is suppressed entirely due to the high inhibition efficiency of the Cu-MBI layer. Furthermore, after the Cu-MBI film decomposes at higher potentials, the remaining Cu_2O and possibly $CuCl/CuCl_2^-$, formed upon doping of cuprous oxide, could be reduced to metallic Cu at sufficient negative potentials during the reverse scan. Based on this, it can be assumed that the C_1 peak would not appear if the degradation of the inhibitor did not occur. This is confirmed for the Cu substrate covered with the polymerised Cu-MBI film [24].

Another set of experiments, including the influence of the potential scanning rate (Fig. 4, Table 2), was performed over the 1–10 mV s^{-1} range. Peak A_1 was well-defined, and peak A_2 appeared like a shoulder, whatever the scan rate. The intensities of peaks A_1, A_2 and A_3, and C_1 fit a linear relationship vs square root of sweep rate ($\nu^{1/2}$) for all samples (Supplementary Figs. S2-S7), with a slight deviation of the intercept from the origin.

Such deviation may be related to electrode roughness or adsorbed species on the surface. The potential of peaks A_1, A_2, A_3 and C_1 also linearly increases with $\nu^{1/2}$. Since both E_p and I_p change linearly with $\nu^{1/2}$, we report that copper corrosion in 3 wt.% NaCl solution, but also the formation of the metal-inhibitor layer (Cu-MBI), obeys the Müller-Casandra passivation model [66]. This is very likely because Cu in chloride solutions forms a layer of insoluble CuCl salt (mc-aq), while MBI forms an insoluble complex with Cu(I) ions forming Cu-MBI (mc-S-aq). It should be noted that mc-P-aq also follows the passivation model, but compared to MBI, OPA does not mitigate copper corrosion but accelerates it, which can be inferred from the increased currents of peaks A_1 and A_2.

3.1.3. X-ray photoelectron spectroscopy

The chemical composition (Table 3), deduced from the survey spectra, showed that control samples (mc-aq and ch-aq) contain high content of Cu and O, which can be attributed to the formation of the oxide layer. Upon exposure to MBI containing aqueous chloride solution (mc-S-aq and ch-S-aq), the concentration of Cu and O at the surface layer diminished together with the trend of increasing concentration of C, N and S. In contrast, phosphorus was not detected on the surface of mc-P-aq and ch-P-aq, which is in line with the electrochemical performance. Table 3 also reveals that the metal-inhibitor complexes did not form on samples modified with inhibitors in EtOH solution.

Fig. 5a displays high-resolution XPS spectra of the Cu 2p core level and the Cu LMM Auger transition for all ten non-inhibited and inhibited copper samples. Results reveal a general tendency for Cu_2O formation, following other reports where preferably Cu(I) oxide was produced on the surface of copper in the chloride solutions [10,58,67]. The Cu $2p_{3/2}$ peak at 932.5 eV could be assigned to Cu_2O, but it is essentially impossible to distinguish between Cu and Cu_2O based on Cu $2p_{3/2}$ photoelectron line measurements because the binding energy for the two is too close to be distinguished within the measured uncertainty [68]. To this end, the intense peak at 570.1 eV in the Auger Cu LMM bands (Fig. 5b) of all samples is an indication that Cu_2O is present on the surface, whereas the contribution of metallic Cu is well-separated by a shift in binding energy (E_b) of 2 eV, i.e., it is at 568.1 eV [69–71]. Copper (II) was not detected in any of the samples due to a lack of strong satellite peaks that would appear in the range 942–947 eV [68] (Fig. 5a). In the Auger spectra of mc-S-aq and ch-S-aq samples, the peaks are broadened, indicating an extra component at about 570.4 eV, probably arising from the formation of a complex between Cu(I) and MBI.

Furthermore, the presence of inhibitor film was corroborated by inspection of N 1s and S 2p spectra (Fig. 5c and d). Nitrogen was detected in all samples treated with the inhibitor (Fig. 5c) but with a significant amount only in mc-S-aq and ch-S-aq. This is consistent with the sulphur content detected only for these two samples. The atomic ratio of N/S is between 2.6 and 2.7 for mc-S-aq and ch-S-aq, which is greater than the stoichiometric ratio of N/S, being 2 for an MBI molecule. The N 1s spectra comprise pyridine (C=N−C) peak at 398.9 eV and pyrrole (C−NH−C) peak at 400.1 eV. The intensity ratio of $I_{pyridine}/I_{pyrrole}$ is almost 1:1 (with a slightly higher pyridine peak) for mc-S-aq, whereas the pyrrole peak is larger than the pyridine peak for ch-S-aq. Such a difference in the ratio between nitrogen components suggests that the MBI bond to copper surfaces differently.

Table 3
Chemical composition (at.%) of the copper surface after 24 h of immersion in: 1) 3 wt.% NaCl with and without the addition of 1 mM 2-mercaptobenzimidazole (S), octylphosphonic acid (P), and 2) ethanolic solution containing S and P followed by immersion in 3 wt.% NaCl. The copper surface before measurements implies: (a) mechanical pre-treatment + deposition of inhibitors from ethanol solution, (b) chemical pre-treatment + deposition from ethanol solution, (c) mechanical pre-treatment + deposition from aqueous solution, and (d) chemical pre-treatment + deposition from aqueous solution.

Sample		mechanical pre-treatment					chemical pre-treatment				
Solution		NaCl	+MBI (S)		+OPA (P)		NaCl	+MBI (S)		+OPA (P)	
Inhibitor medium		aq	EtOH	aq	EtOH	aq	aq	EtOH	aq	EtOH	aq
Elements (at.%)	Cu	45.3	35.8	7	30.8	43.4	40.2	28.2	6.4	28.9	35.1
	O	26.4	25.2	6.5	25.3	19.4	25.5	25.3	8.2	25.2	21.1
	C	27.8	36.2	69.7	40.3	35.4	29.6	42.7	68	42.8	41.5
	Cl	0.5	0.8	–	1.7	–	1.5	–	–	–	–
	N	–	2	12.1	1.9	1.8	3.2	3.8	12.7	3.1	2.3
	S	–	–	4.7	–	–	–	–	4.7	–	–
	P	–	–	–	–	–	–	–	–	–	–

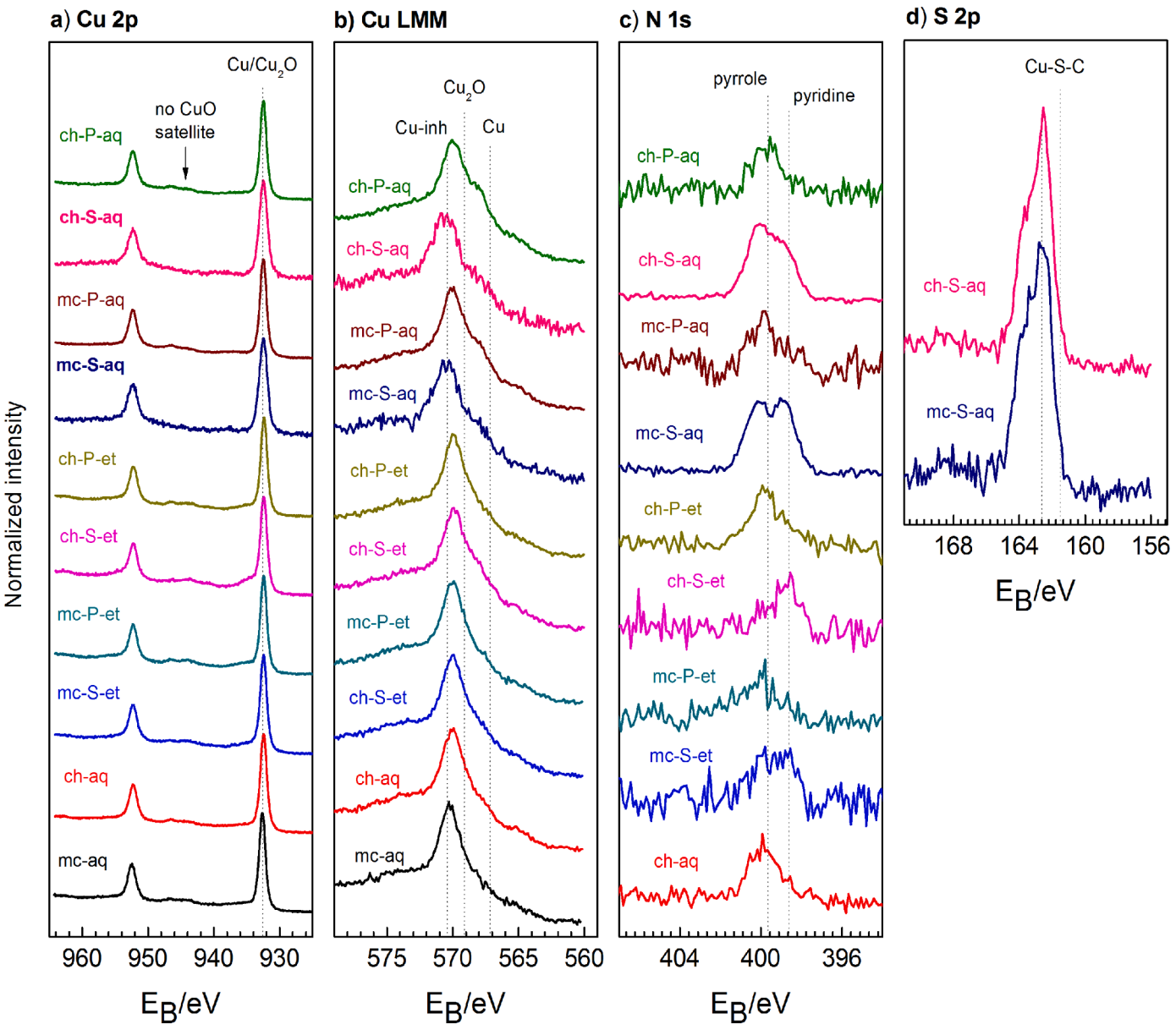

Fig. 5. High-resolution XPS spectra of (a) Cu 2p, (b) Cu LMM, (c) N 1s, and (d) S 2p recorded after immersion of copper in: 1) 3 wt.% NaCl solution for 24 h with and without the addition of 1 mM OPA or MBI, and 2) ethanolic solution containing MBI and OPA followed by immersion in 3 wt. NaCl. The modification of copper surface before XPS measurements implies: mechanical or chemical pre-treatment and deposition of MBI or OPA from ethanol or aqueous solution.

In our previous publications [10,15,21], we showed, by DFT calculations, that the MBI molecules adsorb on the copper surface either as thione or thiolate, with the preference between the two depending on surface details. Furthermore, our XPS results [21] suggested that when the ratio of $I_{pyridine}/I_{pyrrole} = 1$, the MBI molecules adsorb on the copper surface as deprotonated thiolates due to the equal peak contribution of the two chemical states. On the other hand, when the pyrrole peak predominates over pyridine, it indicates that some MBI molecules, in addition to being adsorbed as thiolate, also adsorb as thione [21]. To conclude, in the mc-S-aq sample, the MBI was adsorbed on the copper surface as thiolate, whereas in ch-S-aq, MBI is adsorbed as thiolate and thione. It seems that chemical etching with HNO_3 altered the copper surface.

The sulphur 2p spectra consist of S $2p_{3/2}$ and S $2p_{1/2}$ spin-orbit components that differ by only 1.1 eV with $2p_{3/2}/2p_{1/2}$ intensity ratio of about 2. Both peaks, S $2p_{3/2}$ at 162.5 eV and S $2p_{1/2}$ at 163.6 eV, are attributed to a single chemical state of metal-mercapto compounds, i.e., Cu-S-C bonding [10,19,72].

3.1.4. Scanning electron microscopy coupled with energy-dispersive X-ray spectroscopy

The surfaces of mechanically and chemically pre-treated samples were examined by FE-SEM coupled with EDS to determine the morphology, structure, and composition of the surface layers (Fig. 6). The surface of the mechanically abraded copper immersed in chloride solution (mc-aq) appears to have corroded uniformly (Fig. 6a). Moreover, large chloride-containing aggregates were observed along with the SiC inclusions originating from sandpaper. Deposition of MBI and OPA from ethanolic solution followed by immersion in chloride solution (mc-S-et and mc-P-et) caused significant damage to the copper surface (Supplementary Fig. S8). The compositional analysis showed the presence of chloride-containing corrosion products (Fig. 7a). The copper oxide layer was detected for all five samples that had been mechanically pre-treated (Fig. 7).

In contrast, the deposition of MBI from an aqueous solution containing NaCl (mc-S-aq) leads to significant corrosion protection, which can be inferred from a smooth surface on which traces from the grinding

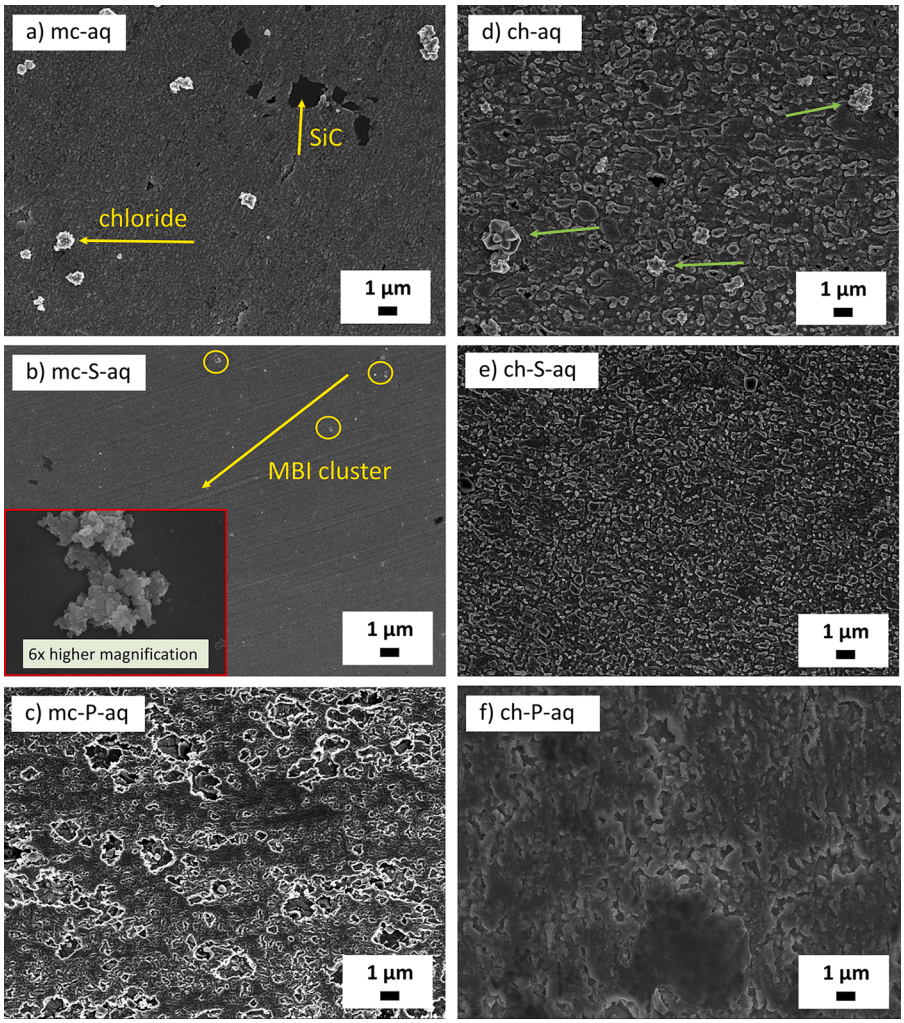

Fig. 6. SEM secondary electron images for copper immersed in 3 wt.% NaCl solution for 24 h with and without adding 1 mM OPA or MBI. The copper surface before recording the images implies: (a) mechanical pre-treatment, (b) mechanical pre-treatment + MBI deposition from aqueous solution, (c) chemical pre-treatment + OPA deposition from aqueous solution, (d) chemical pre-treatment, (e) mechanical pre-treatment + MBI deposition from aqueous solution, (f) chemical pre-treatment + OPA deposition from aqueous solution.

process are still visible (Fig. 6b). In addition, some small clusters may be noticed at higher magnification (the inset in Fig. 6b), which can be attributed to corrosion products at first glance. However, the BSE image and EDS analysis revealed that the cluster originates from an inhibitor since it contains nitrogen and sulphur (Fig. 7b). Also, the cluster contains chlorine which correlates with the polymerised $[Cu\text{-}Cl\text{-}MBI]_n$ structure observed in our previous publication [24] for copper samples treated with an aqueous chloride solution containing a synergistic combination of MBI and OPA. Another inhibitor, OPA, dissolved in an aqueous solution (mc-P-aq), caused severe corrosion of copper (Fig. 6c). Interestingly, chlorine was not detected on the surface of this sample (Fig. 7c). On the other hand, the surface of copper chemically etched (ch-aq) seems to become much rougher (Fig. 6d) than mc-aq. The visible large aggregates marked with green arrows are attributed to the chloride corrosion products.

The chemically pre-treated copper surface after exposure to MBI and OPA solutions, either ethanolic (Supplementary Figs. S8 and S10) or aqueous (Figs. 6 and 8), behave similarly to their counterparts, i.e., mechanically prepared copper samples treated with inhibitors (Figs. 6 and 7, Supplementary Figs.8 and S9). Only ch-S-aq showed the inhibition of corrosion in chloride solution.

The surface of ch-S-aq (Fig. 6e) was less rough than the surface of the control sample (ch-aq), with no visible corrosion products. However, the EDS detected clusters corresponding to MBI (Fig. 8b), as described in the case for mc-S-aq. The oxygen was not detected on the surface covered with the thin Cu-MBI film. Since the surface composition of ch-S-aq is the same as mc-S-aq, the somewhat more pronounced corrosion inhibition of ch-S-aq compared to mc-S-aq can be attributed to a more favourable morphology, i.e., ch-S-aq has a larger surface area. Such observations are consistent with XPS and electrochemical measurements.

3.2. Aluminium

3.2.1. Potentiodynamic polarisation curves

Fig. 9 shows the potentiodynamic curves recorded in 3 wt.% NaCl solution for mechanically and chemically pre-treated aluminium samples. Anodic dissolution of the control sample (mc) occurs without any sign of passivation. The pitting is likely near the E_{corr} (Table 4) due to the interaction of Cl^- with the oxide film [73]. Moreover, the constant perturbations in the anodic curve are probably due to the metastable pitting phenomena [74]. In contrast, a small pseudo-passive region ($\Delta E_{pass} \approx 70$ mV) was observed for ch. The cathodic polarisation curve of mc exhibits a higher contribution of mass transport than that of ch. Fig. 9 also shows the corrosion behaviour of a chemically etched Al sample immersed for 24 h in NaCl. The ch-aq underwent immediate pitting, but the cathodic currents were slightly decreased with no change in OCP compared to the mechanically pre-treated sample, mc-aq (Table 4). These results strongly suggest that the surface morphology and composition of aluminium were modified after chemical pre-treatment by NaOH and HNO_3, as presented by XPS and SEM-EDS results (see below).

Organic films for both pre-treated samples were pre-formed by liquid-phase deposition either from non-aqueous (ethanol) or an

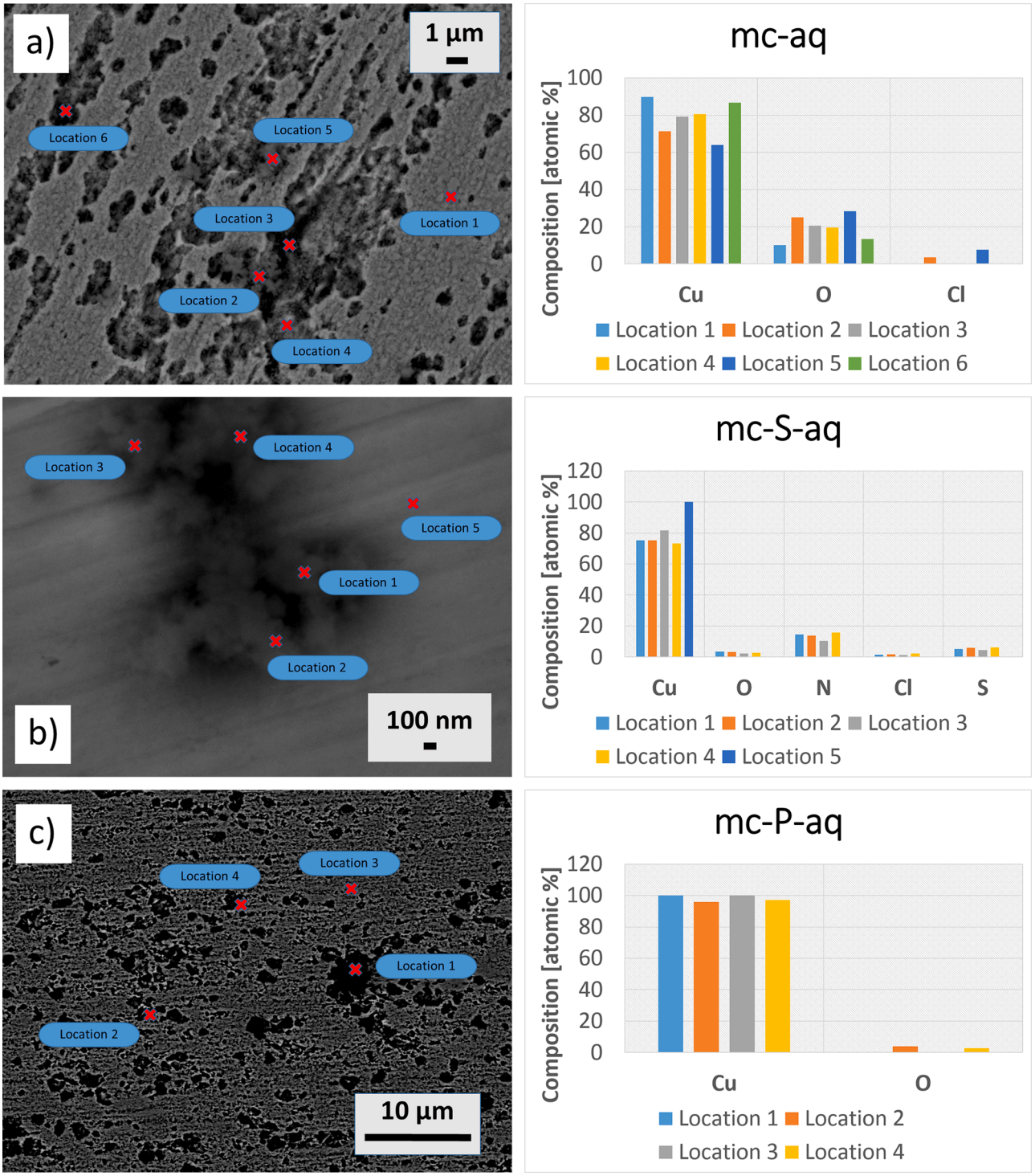

Fig. 7. SEM images recorded in backscattered electron (BSE) mode for copper immersed for 24 h in 3 wt.% NaCl solution with and without adding 1 mM OPA or MBI. The copper surface before recording the images implies: (a) mechanical pre-treatment, (b) mechanical pre-treatment + MBI deposition from aqueous solution, (c) mechanical pre-treatment + OPA deposition from aqueous solution. Locations denoted by a cross mark indicate the spots where EDS analysis was conducted (charts to the right of the SEM images).

aqueous solution containing MBI and OPA. Polarisation curves of the MBI and OPA-modified surfaces in the ethanol solution, mc-S-Et and mc-P-Et, show that both samples behave similarly, i.e., there is no decrease in the current densities compared to mc (Fig. 10a, Table 4).

Such behaviour is explained by the fact that neither MBI nor OPA were adsorbed on the surface of the aluminium substrate, as confirmed by XPS (see below, Table 5). This is in line with the study by Hauffman et al., who reported that ethanol was an unsuitable solvent for the deposition of n-octylphosphonic acid [75]. The authors suggested that the reaction of the phosphonic acids with the aluminium hydroxyls creates a local aqueous environment, which is, in combination with dissolved acids, hazardous to the oxide surface. However, only the ch-P-Et counterpart showed a slight decrease in the corrosion current rate (i.e., a pronounced decrease in the ORR rate) by order of magnitude compared to the control sample, ch (Fig. 10b, Table 4). It is unclear how the OPA affects the surface of an aluminium substrate because the

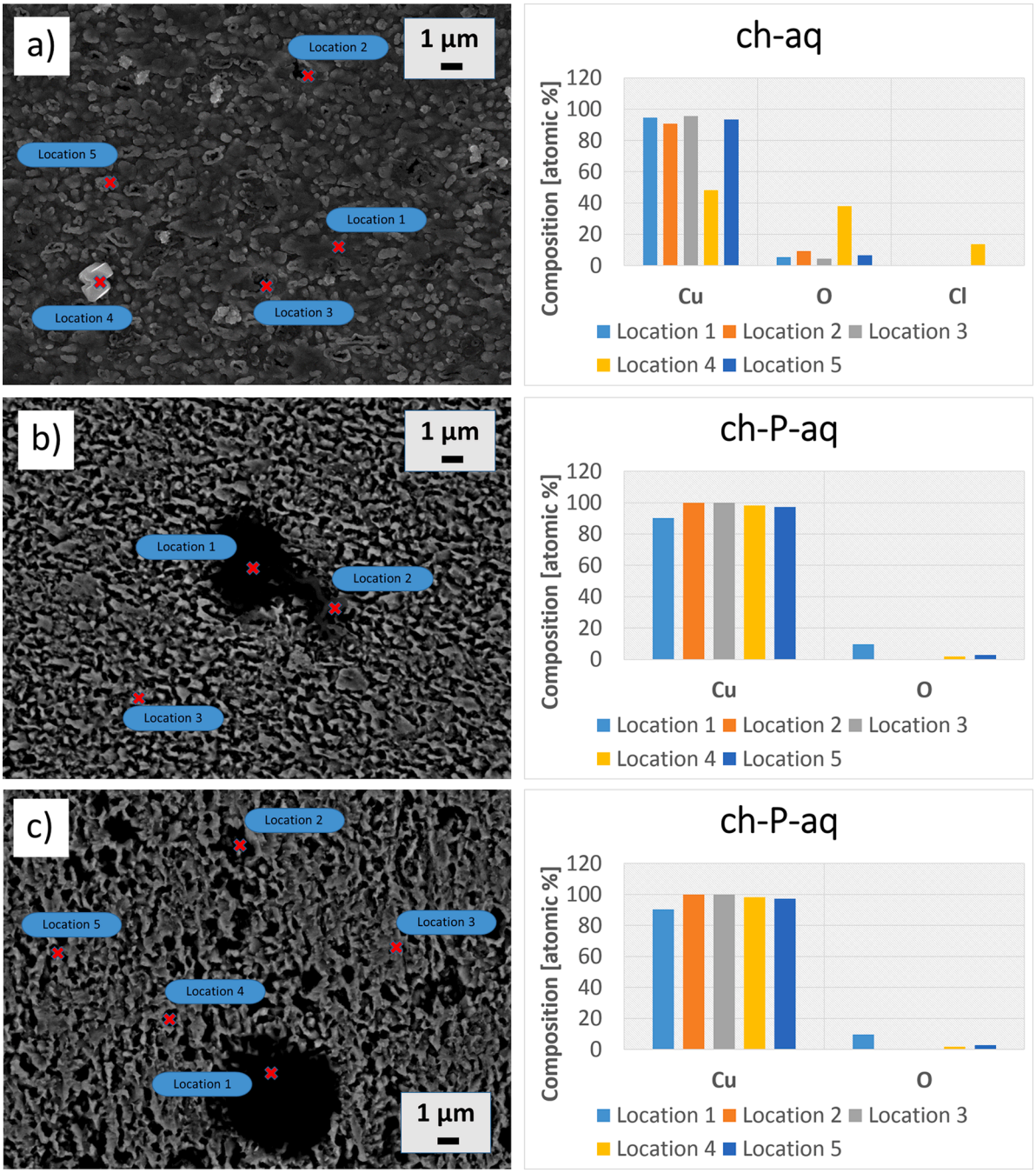

Fig. 8. SEM images recorded in backscattered electron (BSE) mode for copper immersed for 24 h in 3 wt.% NaCl solution with and without adding 1 mM OPA or MBI. The copper surface before recording the images implies: (a) chemical pre-treatment, (b) chemical pre-treatment + MBI deposition from aqueous solution, (c) chemical pre-treatment + OPA deposition from aqueous solution. Locations denoted by a cross mark indicate the spots where EDS analysis was conducted (charts to the right of the SEM images).

chemical composition obtained from the XPS surface measurements showed no phosphorus content. Since neither OPA nor MBI induced passivity in any of the samples (mc-S-Et, mc-P-Et, ch-S-Et and ch-P-Et), they are considered ineffective inhibitors when ethanol is used to deposit the layers.

On the other hand, functionalisation of the Al surface with OPA+NaCl in an aqueous solution, mc-P-aq (Fig. 10c), shows a passivation response (i.e., pseudo-passivation because there is no sharp transition between the active-passive region) [21,48,76] consistent with the suppression of the anodic reaction and with the positive shift in E_{corr}, compared to the control sample, mc-aq. In contrast to mc-S-et, mc-S-aq adsorbed MBI on the Cu surface induced a two-fold reduction of corrosion rate (Fig. 10c, Table 4). Only the ORR was influenced by slight inhibition, whereas immediate pitting occurs already at E_{corr}, which is in line with the surface characterisation results, XPS and EDS (see below). In the presence of MBI (ch-S-aq), the corrosion was accelerated. In contrast, the OPA induces a reduction of corrosion current density (ch-P-aq) relative to the control sample but has almost the same ΔE_{pass} range and the same slope of the pseudo-passive region as for the mc-P-aq (Table 4). The identifiable E_{pit} for ch-P-aq shifts to less active values (i.e., more noble potentials) compared to mc-P-aq. This result may indicate that the role of OPA in mitigating corrosion of aluminium is predominantly as a pitting corrosion inhibitor. It should be noted that although OPA is recognised as a potential corrosion inhibitor for aluminium, it

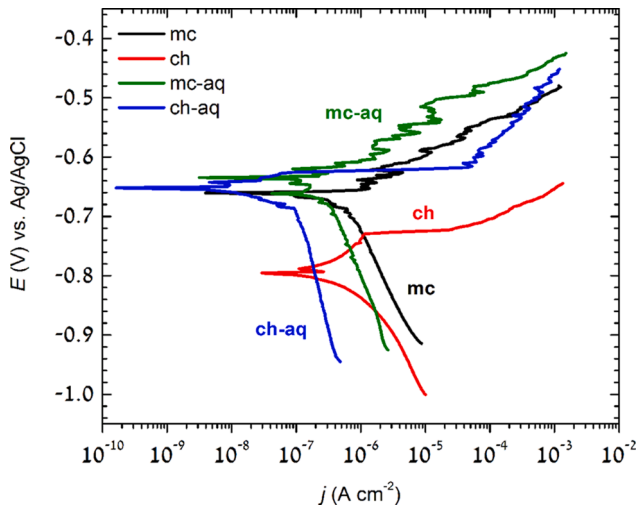

Fig. 9. Potentiodynamic polarisation curves recorded for aluminium samples in 3 wt.% NaCl solution. The aluminium surface before measurements implies mechanical pre-treatment and chemical pre-treatment. The difference between mc (ch) and mc-aq (ch-aq) samples is only immersion time; the former was immersed for 1 h and the latter for 24 h in chloride solution.

offers only moderate inhibition efficiency due to its relatively short octyl chain, which can also be inferred from the pseudo-passive behaviour of the polarisation curve. This observation agrees with the results of Milošev and co-workers [30], which showed that the backbone of the inhibitor molecules is responsible for lateral cohesive interactions, i.e., the elongation of the alkyl chain is beneficial and results in the establishment of a broader pseudo-passivity region.

3.2.2. *X-ray photoelectron spectroscopy*

Table 5 shows that the surface composition of mc-aq differs significantly from ch-aq; during chemical etching, a large portion of adventitious organic compounds is removed, i.e., the content of C is reduced from 39% to 26%, followed by an increase in the content of Al and O. The characteristic peak located at 72.6 eV was assigned to the metallic Al [31,72]. This peak is much more pronounced and shifted by almost 1 eV (i.e., at 71.7 eV) for ch-aq, compared to mc-aq. The Al 2p core-level spectra also present a peak at 74.7 eV assigned to the aluminium oxide and/or hydroxide component [77,78]. Aluminium oxides and hydroxides (Al_2O_3, $Al(OH)_3$ and AlOOH) are extremely difficult to differentiate by XPS because their corresponding E_b values overlap each other [79,80]. However, different hydroxides formed by different pre-treatments could be deduced from the O/Al ratio. This assumption shows that some difference exists between mechanical and chemical pre-treatment. The O/Al ratio for mc-aq is 2.8, compared to the O/Al ratio of 2 for ch-aq. This may indicate that the surface after mechanical pre-treatment consists mainly of $Al(OH)_3$ and that the chemical pre-treatment modified the surface in a way that led to the formation of AlO(OH) or a combination of $Al(OH)_3$ and Al_2O_3. It can be seen from Fig. 11a that all spectra corresponding to the chemical pre-treatment were shifted towards higher E_b values.

After immersion of the pre-treated Al samples in an ethanol solution of OPA, no significant changes can be observed. The most important result is that phosphorus was detected only on the surfaces of the samples exposed to the OPA containing aqueous solution, i.e., mc-P-aq and ch-P-aq (Table 5). Moreover, the organic film of the ch-P-aq contained a higher amount of phosphorus (7.4 at.%) than mc-P-aq (6.2 at.%). The peak maximum at 133.6 eV (Fig. 11b) was related to the metal-phosphonate (P-O-Al) bonding as reported previously [21,25,78,81].

The adsorption of OPA is confirmed by a significant decrease in Al and O content and an increase in the content of C. It is well-known that the presence of oxide/hydroxide on the Al surface is required for the condensation reaction; P-OH + OH-Al* ⟶ P-O-Al* + H_2O, where Al* stands for surface Al ion [30]. Apart from the recorded signal for phosphorus, no sulphur content was detected in any of the samples (Table 5). The adsorption of phosphonate was corroborated by the broadening of the O 1s core-level peaks for mc-P-aq and ch-P-aq (Fig. 11c), indicating the presence of the new component(s), as demonstrated by deconvolution of the high-resolution spectra in our previous work [21]. The peaks centred at 532 eV are ascribed to aluminium oxide/hydroxide species [29,77], whereas the new component(s) between 533 eV and 534 eV correspond to Al-O-P and/or H-O-P [26,78,81].

Fig. 11d shows the C 1s spectra with the peaks at 284.8 eV and around 289 eV attributed to C-H/C-C and C=O/O-C=O groups, respectively, which generally arise from airborne carbonaceous contaminants [29,77,82]. Upon adsorption of OPA inhibitor on Al substrate, the major peak corresponds to the methylene groups of OPA molecule, whereby the signal for oxidised carbon contaminants disappeared. The alkyl chain length strongly influences the molecular packing during film formation. The longer chains adsorb stronger due to an increase in van der Waals attractive forces; the strength of the van der Waals interactions increases with the number of methylene units in adsorbate. Hoque et al. [29] reported that longer chain molecules such as dodecylphosphonic acid (DP) and octadecylphosphonic acid (ODP) formed more densely packed phosphonate self-assembling monolayer on Al surface, unlike octylphosphonic acid. This agrees with the electrochemical results where the mc-P-aq and ch-P-aq did not reach complete passivity or broad pseudo-passivity as in the work of Milošev et al. [30].

Furthermore, Kokalj and Costa [83] analysed, with the aid of computational modelling, the mechanism by which organic self-assembled-monolayers hinder the penetration of Cl^- ions from aqueous solution toward the metal substrate. Their scheme describes the activation barrier for Cl^- penetration into SAM as a function of the electrode potential and shows that the activation barrier decreases as the electrode potential increases. Still, for thick SAMs, the barrier remains sizable, even at more positive potentials. The authors suggested that this might be one of the reasons why dense and sufficiently thick SAMs efficiently inhibit corrosion.

3.2.3. *Scanning electron microscopy coupled with energy-dispersive X-ray spectroscopy*

First, the ground (mechanically pre-treated, mc-aq) and etched (chemically pre-treated, ch-aq) surfaces are compared to get insight into

Table 4
Electrochemical parameters – corrosion potential (E_{corr}), corrosion current density (j_{corr}), pitting potential (E_{pit}), passive range (ΔE_{pass}), passive current density (j_{pass}), anodic Tafel slope (b_a) and cathodic Tafel slope (b_c) – deduced for Al from the potentiodynamic polarisation curves (Figs. 9 and 10). Values for E_{corr} and j_{corr} are given as mean ± standard deviation.

Al samples	E_{corr} ($mV_{Ag/AgCl}$)	j_{corr} (A cm^{-2})	E_{pit} (mV)	ΔE_{pass} (mV)	b_a (mV/dec)	$-b_c$ (mV/dec)
mc-aq	−640 ± 21	(3.13 ± 0.90) × 10^{-7}	–	–	–	243
mc-S-aq	−664 ± 7	(7.70 ± 0.41) × 10^{-8}	–	–	–	186
mc-P-aq	−570 ± 24	(1.52 ± 0.51) × 10^{-8}	−220	330	134	188
ch-aq	−795 ± 4	(1.95 ± 1.73) × 10^{-7}	–	–	–	295
ch-S-aq	−800 ± 11	(6.52 ± 0.67) × 10^{-8}	–	–	–	137
ch-P-aq	−477 ± 15	(2.53 ± 0.77) × 10^{-8}	−120	350	144	150

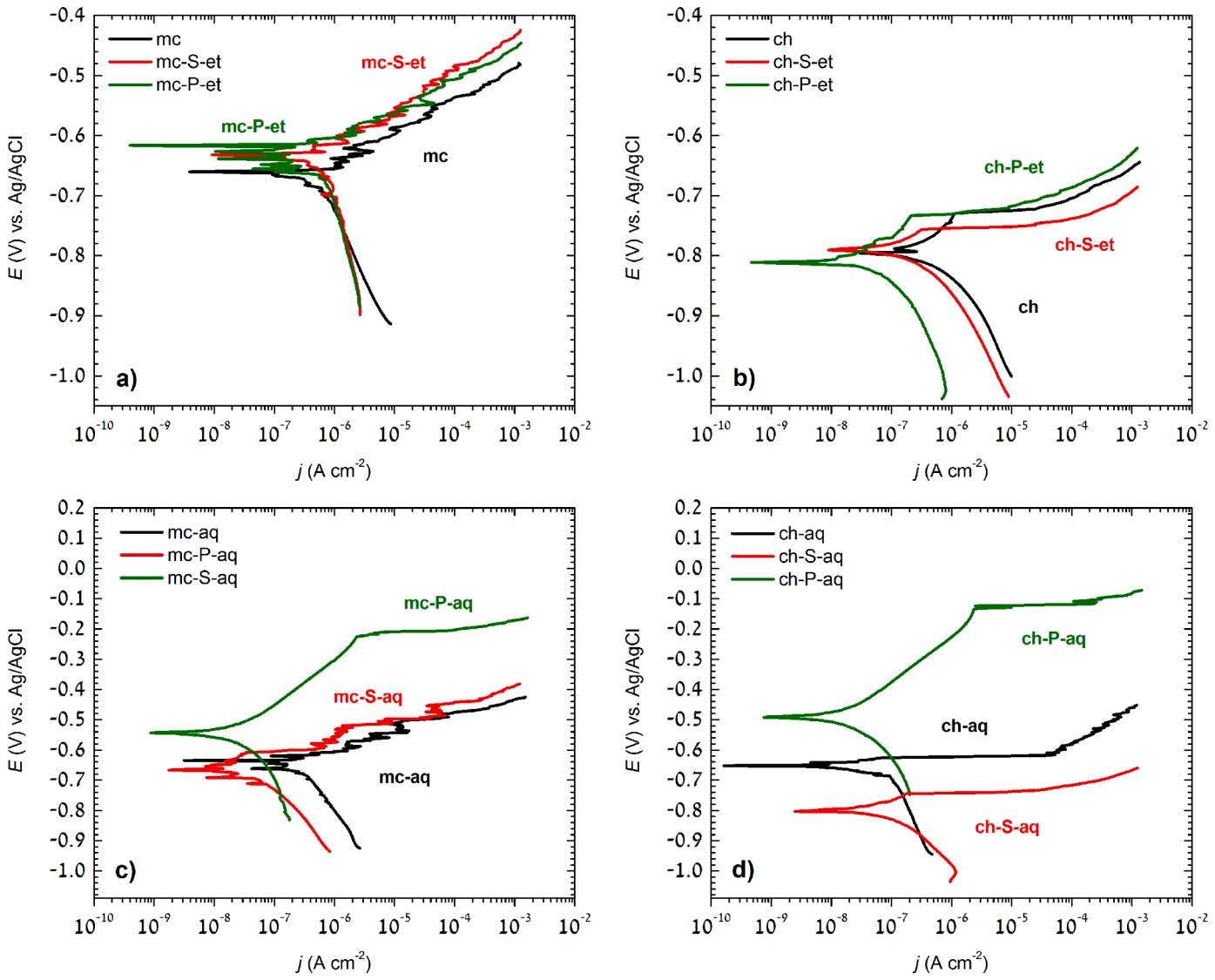

Fig. 10. Potentiodynamic polarisation curves recorded for aluminium in (a and b) 3 wt.% NaCl solution and (c and d) 3 wt.% NaCl with the addition of 1 mM OPA or MBI. The aluminium surface before measurements implies: (a) mechanical pre-treatment + deposition of inhibitors from ethanol solution, (b) chemical pre-treatment + deposition from ethanol solution, (c) mechanical pre-treatment + deposition from aqueous solution, and (d) chemical pre-treatment + deposition from aqueous solution.

Table 5
Chemical composition of the aluminium surface after 24 h of immersion in: 1) 3 wt.% NaCl with and without the addition of 1 mM 2-mercaptobenzimidazole (S), octylphosphonic acid (P), and 2) ethanolic solution containing S and P followed by immersion in 3 wt.% NaCl. The aluminium surface before measurements implies: (a) mechanical pre-treatment + deposition of inhibitors from ethanol solution, (b) chemical pre-treatment + deposition from ethanol solution, (c) mechanical pre-treatment + deposition from aqueous solution, and (d) chemical pre-treatment + deposition from aqueous solution.

Sample		mechanical pre-treatment					chemical pre-treatment				
Solution		NaCl	+MBI (S)		+OPA (P)		NaCl	+MBI (S)		+OPA (P)	
Inhibitor medium		aq	EtOH	aq	EtOH	aq	aq	EtOH	aq	EtOH	aq
Elements	Al	16	19.1	13.9	18.8	7.4	24.3	12.5	16.7	13.9	4
	O	44.4	60.5	43.8	59.2	28.6	49.7	46.6	47.4	47.3	25.6
	C	39.1	19.4	41.9	21.6	57.8	26	39.6	35.9	38.3	63
	Cl	–	1	0.4	0.4	–	–	0.5	–	0.5	–
	N	0.5	–	–	–	–	–	0.8	–	–	–
	S	–	–	–	–	–	–	–	–	–	–
	P	–	–	–	–	6.2	–	–	–	–	–

the potential importance of mild surface preparation of aluminium. The surface of ch-aq (Fig. 12d) was characterised by large roughness with a hemisphere-like appearance compared to mc-aq, which was flat with visible inclusions of corrosion products (Fig. 12a). EDS analysis showed that both surfaces (Figs. 13a and 14a) contained aluminium oxide. In addition, impurities such as SiC and iron particles are distributed over the entire surface. The presence of carbon in all samples originates from the deposited layer before SEM imaging.

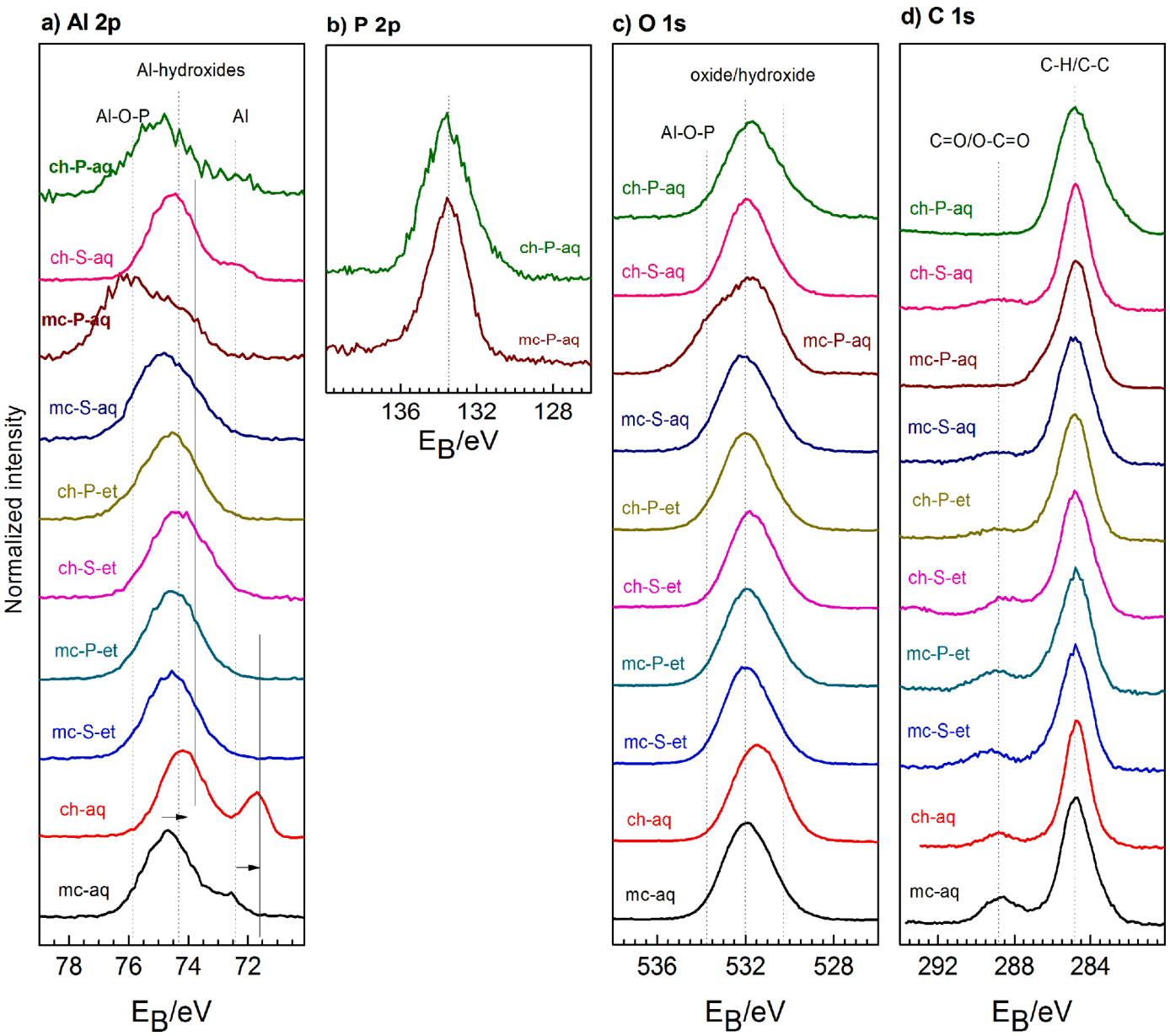

Fig. 11. High-resolution XPS spectra of (a) Al 2p, (b) P 2p, (c) O 1s, and (d) C 1s recorded after 24 h immersion of aluminium in: 1) 3 wt.% NaCl solution with and without the addition of 1 mM OPA or MBI, and 2) ethanolic solution containing MBI and OPA followed by immersion in 3 wt.% NaCl. The modification of aluminium surface before XPS measurements implies: mechanical or chemical pre-treatment and deposition of MBI or OPA either from ethanol or aqueous solution.

After immersion of the mechanically prepared Al sample in an ethanolic solution of MBI (mc-S-et, Fig. S11a) and OPA (mc-P-et, Supplementary Fig. S11b), no significant changes were observed except that the particles belonging to the corrosion products were larger compared to the control sample (mc-aq). Also, when the chemically prepared Al samples were immersed in the ethanolic solution of MBI (ch-S-et, S11c) and OPA (ch-P-et, Fig. S11d), the shape and composition (Figs. S12 and S13) of the hemispheres did not change relative to the control sample (ch-aq), indicating no inhibition of the corrosion processes which is consistent with the electrochemical and XPS results.

In contrast, when an aqueous NaCl solution was used as a solvent of choice instead of ethanol, events on the aluminium surface changed drastically. To this end, let us compare the SEM micrographs for mechanically and chemically pre-treated surfaces immersed in an aqueous MBI and OPA-containing chloride solution. The mc-S-aq surface is slightly damaged over the entire surface (Fig. 12b), but galvanic corrosion and locally attacked sites, appear to occur at the edges of very large iron particles[1], as confirmed by EDS analysis (Fig. 13b). It is difficult to notice a difference in surface appearance between ch-S-aq (Fig. 12e) and the control sample (ch-aq) (Fig. 12d), while the clear difference exist between ch-S-aq and mc-S-aq (Fig. 13b). In addition, it is evident that ch-S-aq has fewer Fe particles (Fig. 14b) compared to its counterpart sample mc-S-aq (Fig. 13b). The corrosion inhibition effect was observed only for OPA inhibitor in aqueous solutions containing chlorides, such as mc-P-aq and ch-P-aq. The morphology of mc-P-aq shows that the scratches from the grinding process are not visible due to the coverage of almost the entire surface by inhibitor particles

[1] Iron particles represent metal impurities of low solubility in aluminium metal. It is the most pervasive impurity element in Al alloys, which stems from the bauxite ore and steel tools used during primary and secondary production [84]. In terms of galvanic series, iron is more noble to aluminium and thus these particles represent electrochemically different sites from Al matrix (sites of cathodic reaction).

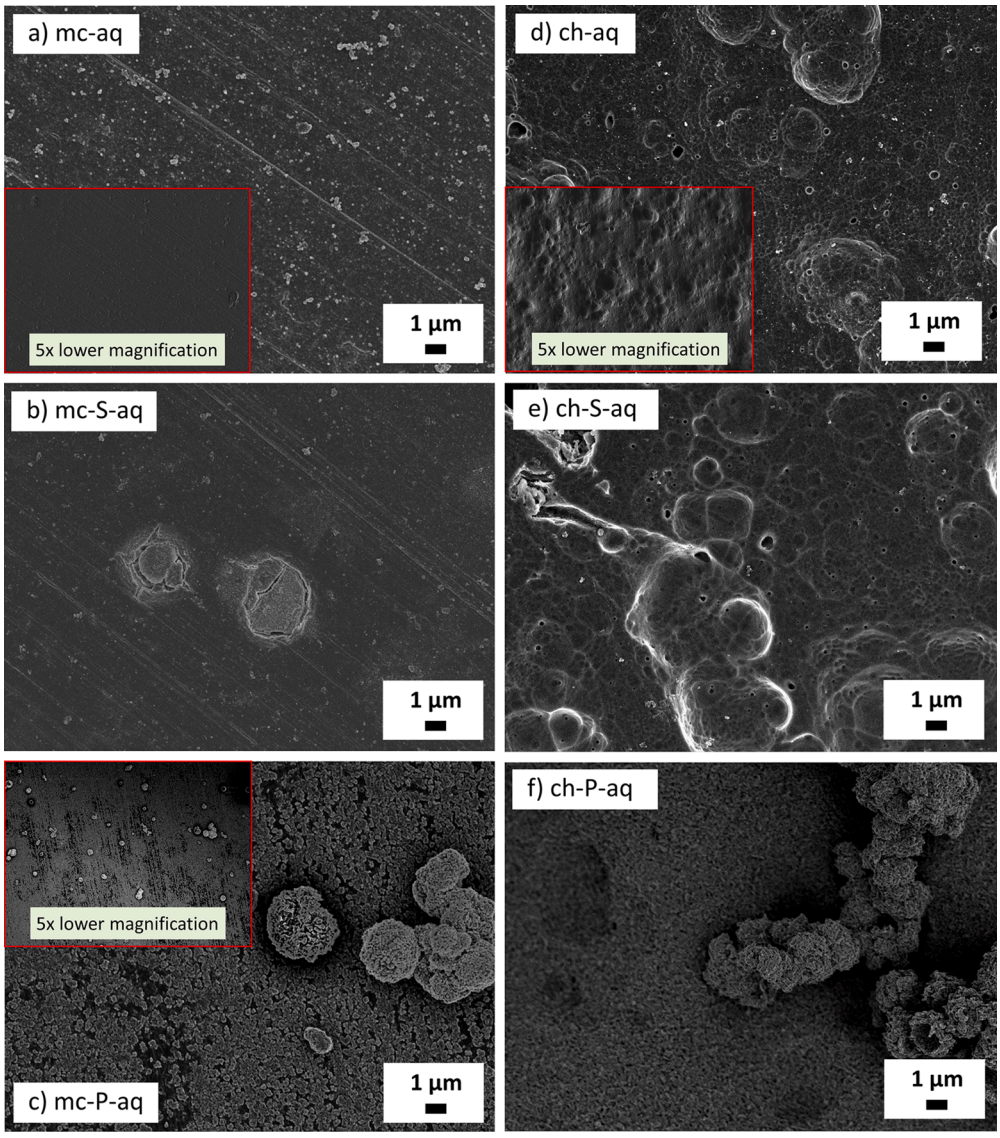

Fig. 12. SEM secondary electron images for aluminium immersed for 24 h in 3 wt.% NaCl solution with and without adding 1 mM OPA or MBI. The aluminium surface before recording the images implies: (a) mechanical pre-treatment, (b) mechanical pre-treatment + MBI deposition from aqueous solution, (c) chemical pre-treatment + OPA deposition from aqueous solution, (d) chemical pre-treatment, (e) mechanical pre-treatment + MBI deposition from aqueous solution, (f) chemical pre-treatment + OPA deposition from aqueous solution.

(Fig. 12c). In addition, large OPA clusters were observed, which was confirmed with EDS analysis where phosphorus was detected (Fig. 13c). It is imperative to highlight that the phosphorus signal was detected only at locations where the OPA agglomerates are formed but not at locations where the thin OPA film was formed. Such a result was expected because the sampling depth of EDS is within the first few micrometres, while the XPS allows the measurement of surface composition within a few nanometres.

The surface of ch-P-aq (Fig. 12f) is even more densely covered with the OPA inhibitor compared to mc-P-aq, which led to a less rough surface compared to the control sample (ch-aq) (Fig. 12d). It appears that ch-P-aq (Fig. 14c) contains more OPA clusters than mc-P-aq (Fig. 13c), as shown by EDS results. The more densely packed OPA on the Al surface recorded with SEM-EDS is consistent with the higher phosphorus content detected by XPS and lower corrosion current rates of ch-P-aq compared to mc-P-aq.

4. Conclusions

The corrosion behaviour of mechanically (mc) and chemically (ch) pre-treated copper and aluminium samples (i.e., control bare samples) was investigated by electrochemical and surface-analytical characterisation means in 3 wt.% NaCl solution. The curves recorded for both control samples for Cu show similar electrochemical characteristics; therefore, the influence of the surface pre-treatment on the bare samples is neglected. On the other hand, the polarisation curves for Al showed that the ORR was slightly inhibited on the chemically pre-treated sample compared to the mechanically pre-treated one.

Organic films for both types of pre-treated samples were prepared by liquid-phase deposition either from ethanol (et) or aqueous (aq) solution containing MBI (S) and OPA (P) inhibitors. The potentiodynamic measurements, measured in 3 wt.% NaCl, revealed that the current density responses on the Cu surface for the samples deposited from ethanol solutions (mc-S-Et and mc-P-Et, ch-S-Et and ch-P-Et) were similar to the control samples mc and ch. The XPS study confirmed that the inhibitor films were not formed in ethanolic solutions and that the Cu-MBI films were formed only after the deposition from an aqueous NaCl solution containing the MBI inhibitor. The polarisation curves for mc-S-aq and ch-S-aq showed a significant reduction in the j_{corr} by almost four orders of magnitude together with the shift of the E_{corr} more positive than the control samples mc-aq and ch-aq. Hence, MBI is considered an effective corrosion inhibitor for Cu in chloride environments for both mechanically and chemically pre-treated surface. The degradation mechanism of Cu-MBI was resolved by the peaks fitting of the cyclic voltammogram of Cu-S-aq, revealing the two peaks within the enlarged peak corresponding to Cu^{2+} and $(MBI)_2$.

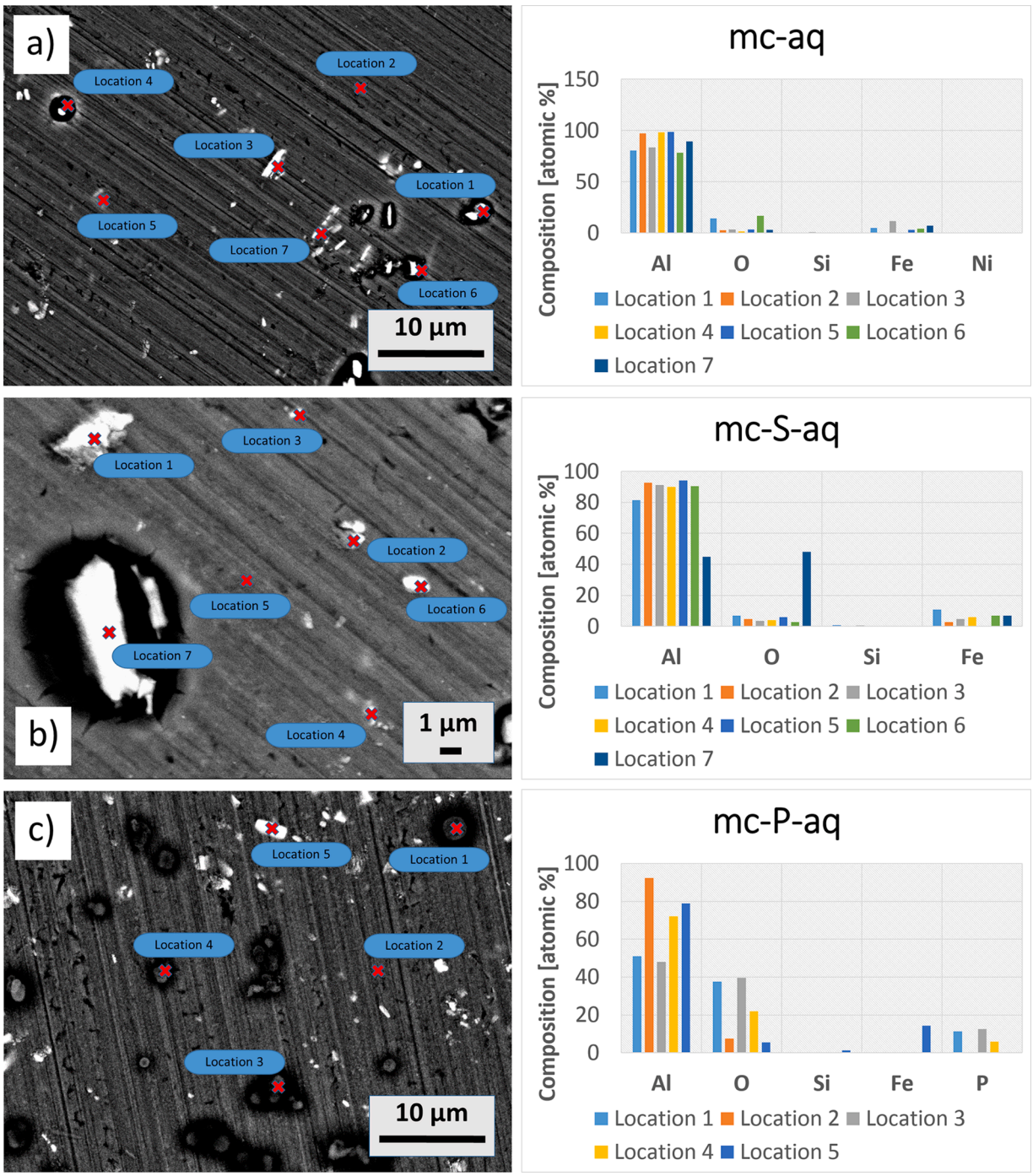

Fig. 13. SEM images recorded in backscattered electron (BSE) mode for copper immersed for 24 hin 3 wt.% NaCl solution with and without adding 1 mM OPA or MBI. The copper surface before recording the images implies: (a) mechanical pre-treatment, (b) mechanical pre-treatment + MBI deposition from aqueous solution, (c) mechanical pre-treatment + OPA deposition from aqueous solution. Locations denoted by a cross mark indicate the spots where EDS analysis was conducted (charts to the right of the SEM images).

The inhibition chemistries of aluminium in aqueous solutions were opposite to those of copper; only the Cu-OPA layer was identified by XPS and confirmed by potentiodynamic polarisation measurements. The polarisation curves for mc-P-aq and ch-P-aq showed a pseudo-passivation response with the shift in E_{pit} to less active values and a positive shift in E_{corr} compared to the control sample. Admittedly, the E_{pit} was slightly higher for ch-P-aq than mc-P-aq. Although OPA is a potential corrosion inhibitor for aluminium, it offers only moderate inhibition efficiency due to its relatively short octyl chain.

Overall, the results showed that the surface pre-treatment did not significantly influence the chemistries of copper and aluminium. However, the film preparation method was crucial, i.e., the inhibitor film was only formed from inhibitor-containing aqueous solutions due to the availability of Cu^{+} ions to form Cu(I)-inhibitor protective layer.

CRediT authorship contribution statement

Dževad K. Kozlica: Methodology, Formal analysis, Writing – review & editing. **Ingrid Milošev:** Conceptualization, Supervision, Methodology, Writing – review & editing.

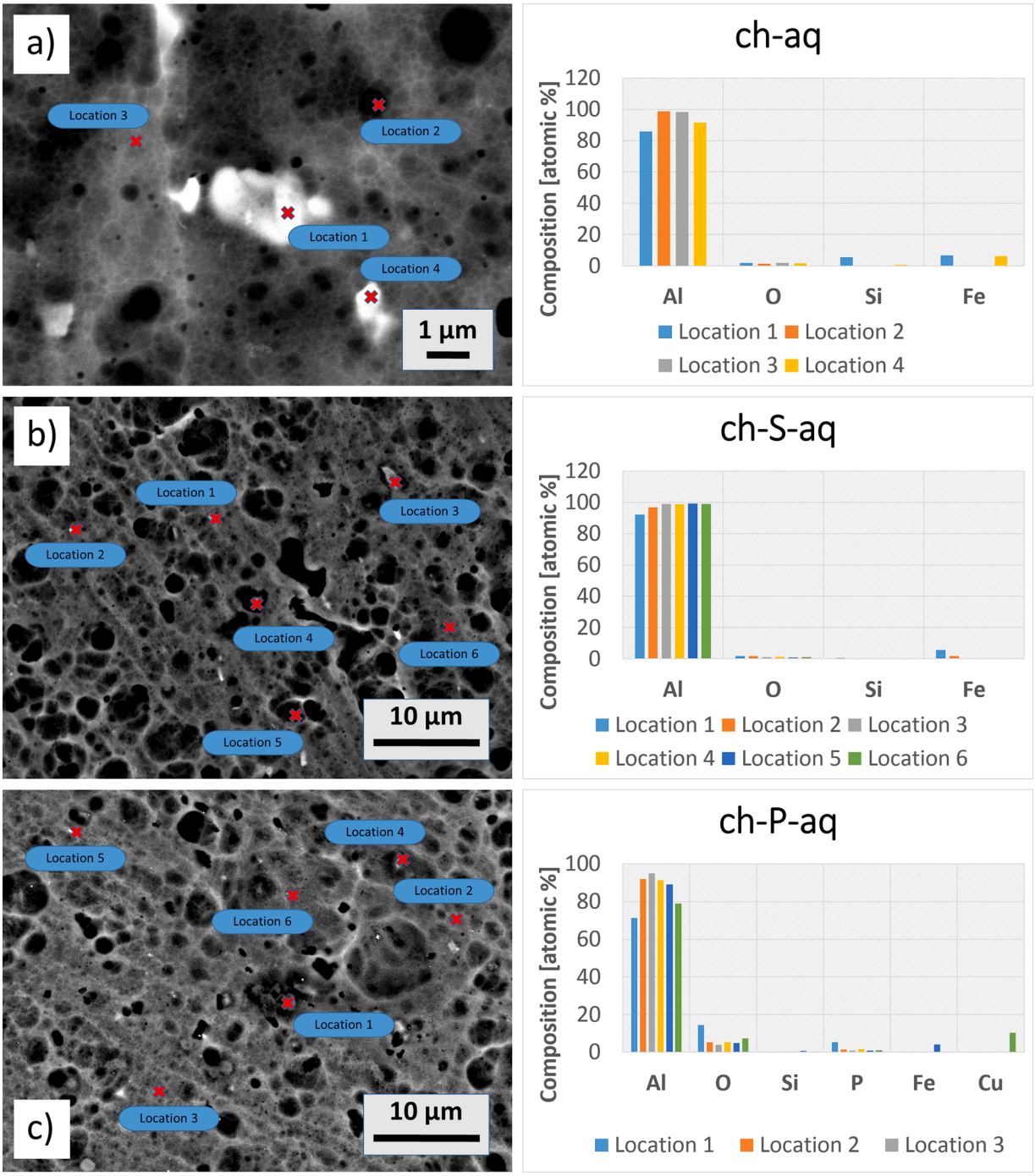

Fig. 14. SEM images recorded in backscattered electron (BSE) mode for aluminium immersed for 24h in 3 wt.% NaCl solution with and without adding 1 mM OPA or MBI. The aluminium surface before recording the images implies: (a) chemical pre-treatment, (b) chemical pre-treatment + MBI deposition from aqueous solution, (c) chemical pre-treatment + OPA deposition from aqueous solution. Locations denoted by a cross mark indicate the spots where EDS analysis was conducted (charts to the right of the SEM images).

Declaration of Competing Interest

The authors declare that they have no known competing financial interests or personal relationships that could have appeared to influence the work reported in this paper.

Data Availability

Data will be made available on request.

Acknowledgments

D. K. K. expresses his gratitude to the Ad Futura for providing the PhD scholarship through the Public scholarship, development, disability and maintenance fund of the Republic of Slovenia (grant no. 11011-116/2017-13). The authors acknowledge the financial support from the Slovenian Research Agency (research core funding No. P2-0393 and No. P1-0134). Barbara Kapun, BSc, is acknowledged for her valuable contribution to performing the SEM/EDS analyses and Centre for Electron Microscopy and Microanalysis of the Jožef Stefan Institute for using

SEM/EDS equipment. The authors also thank dr. Janez Kovač of the Department of Surface Engineering and Optoelectronics for the XPS analysis.

Supplementary materials

Supplementary material associated with this article can be found, in the online version, at doi:10.1016/j.electacta.2022.141154.

References

[1] P. Schmutz, G.S. Frankel, Corrosion study of AA2024-T3 by scanning Kelvin probe force microscopy and in situ atomic force microscopy scratching, J. Electrochem. Soc. 145 (1998) 2295, https://doi.org/10.1149/1.1838634.

[2] T. Dursun, C. Soutis, Recent developments in advanced aircraft aluminium alloys, Mater. Des. 56 (2014) 862–871, https://doi.org/10.1016/j.matdes.2013.12.002.

[3] Z. Huda, N.I. Taib, T. Zaharinie, Characterization of 2024-T3: an aerospace aluminum alloy, Mater. Chem. Phys. 113 (2009) 515–517, https://doi.org/10.1016/j.matchemphys.2008.09.050.

[4] A.E. Hughes, A.M. Glenn, N. Wilson, A. Moffatt, A.J. Morton, R.G. Buchheit, A consistent description of intermetallic particle composition: an analysis of ten batches of AA2024-T3, Surf. Interface Anal. 45 (10) (2013) 1558–1563, https://doi.org/10.1002/sia.5207.

[5] A. Boag, R.J. Taylor, T.H. Muster, N. Goodman, D. McCulloch, C. Ryan, B. Rout, D. Jamieson, A.E. Hughes, Stable pit formation on AA2024-T3 in a NaCl environment, Corros. Sci 52 (2010) 90–103, https://doi.org/10.1016/j.corsci.2009.08.043.

[6] M. Costa, C.B. Klein, Toxicity and carcinogenicity of chromium compounds in humans, Crit. Rev. Toxicol. 36 (2006) 155–163, https://doi.org/10.1080/10408440500534032.

[7] O. Gharbi, S. Thomas, C. Smith, N. Birbilis, Chromate replacement: what does the future hold? Npj Mater. Degrad. 2 (2018) 23–25, https://doi.org/10.1038/s41529-018-0034-5.

[8] V.S. Sastri, Green Corrosion Inhibitors: Theory and Practice, John Wiley & Sons, 2011, https://doi.org/10.1002/9781118015438.

[9] I. Milošev, Contemporary modes of corrosion protection and functionalization of materials, Acta Chim. Slov. 66 (2019) 511–533, https://doi.org/10.17344/acsi.2019.5162.

[10] I. Milošev, N. Kovačević, J. Kovač, A. Kokalj, The roles of mercapto, benzene and methyl groups in the corrosion inhibition of imidazoles on copper: I. Experimental characterization, Corros. Sci. 98 (2015) 107–118, https://doi.org/10.1016/j.corsci.2015.05.006.

[11] J. Li, C.W. Du, Z.Y. Liu, X.G. Li, M. Liu, Inhibition film formed by 2-mercapto-benzothiazole on copper surface and its degradation mechanism in sodium chloride solution, Int. J. Electrochem. Sci. 11 (2016) 10690–10705, https://doi.org/10.20964/2016.12.46.

[12] I. Dugdale, J.B. Cotton, An electrochemical investigation on the prevention of staining of copper by benzotriazole, Corros. Sci. 3 (1963) 69–74, https://doi.org/10.1016/S0010-938X(63)80001-3.

[13] M. Finšgar, 2-Mercaptobenzimidazole as a copper corrosion inhibitor: part I. Long-term immersion, 3D-profilometry, and electrochemistry, Corros. Sci. 72 (2013) 82–89, https://doi.org/10.1016/j.corsci.2013.03.011.

[14] J. Izquierdo, J.J. Santana, S. González, R.M. Souto, Uses of scanning electrochemical microscopy for the characterization of thin inhibitor films on reactive metals: the protection of copper surfaces by benzotriazole, Electrochim. Acta. 55 (2010) 8791–8800, https://doi.org/10.1016/j.electacta.2010.08.020.

[15] N. Kovačević, I. Milošev, A. Kokalj, The roles of mercapto, benzene, and methyl groups in the corrosion inhibition of imidazoles on copper: II. Inhibitor-copper bonding, Corros. Sci. 98 (2015) 457–470, https://doi.org/10.1016/j.corsci.2015.05.041.

[16] M. Finšgar, I. Milošev, Inhibition of copper corrosion by 1,2,3-benzotriazole: a review, Corros. Sci. 52 (2010) 2737–2749, https://doi.org/10.1016/j.corsci.2010.05.002.

[17] G. Žerjav, I. Milošev, Protection of copper against corrosion in simulated urban rain by the combined action of benzotriazole, 2-mercaptobenzimidazole and stearic acid, Corros. Sci. 98 (2015) 180–191, https://doi.org/10.1016/j.corsci.2015.05.023.

[18] G. Xue, X.Y. Huang, J. Dong, J. Zhang, The formation of an effective anti-corrosion film on copper surfaces from 2-mercaptobenzimidazole solution, J. Electroanal. Chem. 310 (1991) 139–148, https://doi.org/10.1016/0022-0728(91)85257-P.

[19] M. Finšgar, 2-Mercaptobenzimidazole as a copper corrosion inhibitor: part II. Surface analysis using X-ray photoelectron spectroscopy, Corros. Sci. 72 (2013) 90–98, https://doi.org/10.1016/j.corsci.2013.03.010.

[20] X. Wu, F. Wiame, V. Maurice, P. Marcus, 2-mercaptobenzimidazole films formed at ultra-low pressure on copper: adsorption, thermal stability and corrosion inhibition performance, Appl. Surf. Sci. 527 (2020), 146814, https://doi.org/10.1016/j.apsusc.2020.146814.

[21] D.K. Kozlica, A. Kokalj, I. Milošev, Synergistic effect of 2-mercaptobenzimidazole and octylphosphonic acid as corrosion inhibitors for copper and aluminium—an electrochemical, XPS, FTIR and DFT study, Corros. Sci. 182 (2021), 109082, https://doi.org/10.1016/j.corsci.2020.109082.

[22] F. Chiter, D. Costa, V. Maurice, P. Marcus, Adsorption of 2-mercaptobenzimidazole corrosion inhibitor on copper: DFT study on model oxidized interfaces, J. Electrochem. Soc. 167 (2020), 161506, https://doi.org/10.1149/1945-7111/abcd4f.

[23] J. Izquierdo, J.J. Santana, S. González, R.M. Souto, Scanning microelectrochemical characterization of the anti-corrosion performance of inhibitor films formed by 2-mercaptobenzimidazole on copper, Prog. Org. Coat. 74 (2012) 526–533, https://doi.org/10.1016/j.porgcoat.2012.01.019.

[24] D.K. Kozlica, J. Ekar, J. Kovač, I. Milošev, Roles of chloride ions in the formation of corrosion protective films on copper, J. Electrochem. Soc. 168 (2021), 031504, https://doi.org/10.1149/1945-7111/abe34a.

[25] E. Hoque, J.A. DeRose, B. Bhushan, K.W. Hipps, Low adhesion, non-wetting phosphonate self-assembled monolayer films formed on copper oxide surfaces, Ultramicroscopy 109 (2009) 1015–1022, https://doi.org/10.1016/j.ultramic.2009.03.033.

[26] R. Zhao, P. Rupper, S. Gaan, Recent development in phosphonic acid-based organic coatings on aluminum, Coatings 7 (2017) 133, https://doi.org/10.3390/coatings7090133.

[27] A. Mahapatro, T.D. Matos Negrón, A. Nguyen, Spectroscopic evaluations of interfacial oxidative stability of phosphonic nanocoatings on magnesium, J. Spectrosc. (2015), https://doi.org/10.1155/2015/350630, 2015.

[28] K. Wapner, M. Stratmann, G. Grundmeier, Structure and stability of adhesion promoting aminopropyl phosphonate layers at polymer/aluminium oxide interfaces, Int. J. Adhes. Adhes. 28 (2008) 59–70, https://doi.org/10.1016/j.ijadhadh.2007.05.001.

[29] E. Hoque, J.A. Derose, G. Kulik, P. Hoffmann, H.J. Mathieu, B. Bhushan, Alkylphosphonate modified aluminum oxide surfaces, J. Phys. Chem. B 110 (2006) 10855–10861, https://doi.org/10.1021/jp061327a.

[30] I. Milošev, D. Zimerl, C. Carriére, S. Zanna, A. Seyeux, J. Iskra, S. Stavber, F. Chiter, M. Poberžnik, D. Costa, A. Kokalj, P. Marcus, The effect of anchor group and alkyl backbone chain on performance of organic compounds as corrosion inhibitors for aluminum investigated using an integrative experimental-modeling approach, J. Electrochem. Soc. 167 (2020), 061509, https://doi.org/10.1149/1945-7111/ab829d.

[31] I. Milošev, T. Bakarič, S. Zanna, A. Seyeux, P. Rodič, M. Poberžnik, F. Chiter, P. Cornette, D. Costa, A. Kokalj, P. Marcus, Electrochemical, surface-analytical, and computational DFT study of alkaline etched aluminum modified by carboxylic acids for corrosion protection and hydrophobicity, J. Electrochem. Soc. 166 (2019) C3131, https://doi.org/10.1149/2.0181911jes.

[32] A.M.A. Mohamed, A.M. Abdullah, N.A. Younan, Corrosion behavior of superhydrophobic surfaces: a review, Arab. J. Chem. 8 (2015) 749–765, https://doi.org/10.1016/j.arabjc.2014.03.006.

[33] S. Hu, Z. Chen, X. Guo, Inhibition effect of three-dimensional (3D) nanostructures on the corrosion resistance of 1-dodecanethiol self-assembled monolayer on copper in NaCl solution, Materials (Basel) 11 (2018) 1225, https://doi.org/10.3390/ma11071225.

[34] I. Maege, E. Jaehne, A. Henke, H.J.P. Adler, C. Bram, C. Jung, M. Stratmann, Self-assembling adhesion promoters for corrosion resistant metal polymer interfaces, Prog. Org. Coat. 34 (1997) 1–12, https://doi.org/10.1016/S0300-9440(98)00010-1.

[35] J.T. Woodward, A. Ulman, D.K. Schwartz, Self-assembled monolayer growth of octadecylphosphonic acid on mica, Langmuir (1996) 12, https://doi.org/10.1021/la9510689.

[36] J.T. Woodward, D.K. Schwartz, In situ observation of self-assembled monolayer growth, J. Am. Chem. Soc. 118 (1996) 10944, https://doi.org/10.1021/ja961524v.

[37] I. Doudevski, W.A. Hayes, D.K. Schwartz, Submonolayer island nucleation and growth kinetics during self-assembled monolayer formation, Phys. Rev. Lett. 81 (1998) 4927, https://doi.org/10.1103/PhysRevLett.81.4927.

[38] C. Messerschmidt, D.K. Schwartz, Growth mechanisms of octadecylphosphonic acid self-assembled monolayers on sapphire (corundum): evidence for a quasi-equilibrium triple point, Langmuir 17 (2001) 462–467, https://doi.org/10.1021/la001266m.

[39] X. Yang, D. Wang, Z. Sun, H. Tang, Adsorption of phosphate at the aluminum (hydr)oxides-water interface: role of the surface acid-base properties, Colloids Surfaces A Physicochem. Eng. Asp. 297 (2007) 84–90, https://doi.org/10.1016/j.colsurfa.2006.10.028.

[40] Z. Feng, Y. Liu, T. Hashimoto, G.E. Thompson, X. Zhou, P. Skeldon, Influence of surface pretreatments on the corrosion protection of sol-gel coated AA2024-T3 aluminium alloy, Surf. Interface Anal. 45 (2013) 1452–1456, https://doi.org/10.1002/sia.5216.

[41] L. Li, A.L. Desouza, G.M. Swain, Effect of deoxidation pretreatment on the corrosion inhibition provided by a trivalent chromium process (TCP) conversion coating on AA2024-T3, J. Electrochem. Soc. 161 (2014) C246, https://doi.org/10.1149/2.031405jes.

[42] B.A. Abd-El-Naby, O.A. Abdullatef, H.M. El-Kshlan, E. Khamis, M.A. Abd-El-Fatah, Effect of alkaline etching on the inhibition of the acidic corrosion of aluminum by lupine extract, Port. Electrochim. Acta. 33 (2015) 1–11, https://doi.org/10.4152/pea.201501001.

[43] S.G. Prolongo, A. Ureña, Effect of surface pre-treatment on the adhesive strength of epoxy-aluminium joints, Int. J. Adhes. Adhes. 29 (2009) 23–31, https://doi.org/10.1016/j.ijadhadh.2008.01.001.

[44] S. Maddela, M.J. O'Keefe, V.C.M. Wang, H.H. Kuo, Influence of surface pretreatment on coating morphology and corrosion performance of ceriumbased conversion coatings on AZ91D alloy, Corrosion 66 (2010), 115006, https://doi.org/10.5006/1.3516220.

[45] G.W. Critchlow, D.M. Brewis, Review of surface pretreatments for aluminium alloys, Int. J. Adhes. Adhes. 16 (1996) 255–275, https://doi.org/10.1016/S0143-7496(96)00014-0.
[46] U. Tiringer, J. Kovač, I. Milošev, Effects of mechanical and chemical pre-treatments on the morphology and composition of surfaces of aluminium alloys 7075-T6 and 2024-T3, Corros. Sci. 119 (2017) 46–59, https://doi.org/10.1016/j.corsci.2017.02.018.
[47] G. Žerjav, I. Milošev, Carboxylic acids as corrosion inhibitors for Cu, Zn and brasses in simulated urban rain, Int. J. Electrochem. Sci. 9 (2014) 2696–2715.
[48] T. Hauffman, O. Blajiev, J. Snauwaert, C. Van Haesendonck, A. Hubin, H. Terryn, Study of the self-assembling of n-octylphosphonic acid layers on aluminum oxide, Langmuir 24 (2008) 13450–13456, https://doi.org/10.1021/la801978a.
[49] R.G. Kelly, J.R. Scully, D.W. Shoesmith, R.G. Buchheit, Electrochemical Techniques in Corrosion Science and Engineering, Marcel Dekker, Inc., New York, 2003.
[50] D.G. Enos, L.L. Scribner, The Potentiodynamic Polarization Scan, Cent. Electrochem. Sci. Eng. 33 (1997), https://doi.org/10.1007/978-1-4614-8933-7.
[51] E. McCafferty, Introduction to Corrosion Science, Springer Science & Business Media, New York, 2010.
[52] P.J. Cumpson, Guide to smoothing in AES and XPS, 1998.
[53] D. Tromans, R.H. Sun, Anodic polarization behavior of copper in aqueous chloride/benzotriazole solutions, J. Electrochem. Soc. 138 (1991) 3225–3244, https://doi.org/10.1149/1.2085397.
[54] M. Braun, K. Nobe, Electrodissolution kinetics of copper in acidic chloride solutions, J. Electrochem. Soc. 126 (1979) 1666, https://doi.org/10.1149/1.2128773.
[55] A.L. Bacarella, J.C. Griess, The anodic dissolution of copper in flowing sodium chloride solutions between 25° and 175 °C, J. Electrochem. Soc. 120 (1973) 459, https://doi.org/10.1149/1.2403477.
[56] F. Hunkeler, G.S. Frankel, H. Bohni, On the mechanism of localized corrosion, Corrosion 43 (1987) 189–191, https://doi.org/10.5006/1.3583134.
[57] M. Liu, J. Li, In-situ Raman characterization of initial corrosion behavior of copper in neutral 3.5% (wt.) NaCl solution, Materials (Basel) 12 (2019) 2164, https://doi.org/10.3390/ma12132164.
[58] A. El Warraky, H.A. El Shayeb, E.M. Sherif, Pitting corrosion of copper in chloride solutions, Anti-Corrosion Methods Mater 51 (2004) 52–61, https://doi.org/10.1108/00035590410512735.
[59] N. Benzbiria, M. Zertoubi, M. Azzi, Influence of copper surface pretreatment on the kinetics of oxygen reduction reaction in 0.5 M NaCl solution: surface characterization and electrochemical studies, Appl. Surf. Sci. Adv. 4 (2021), 100069, https://doi.org/10.1016/j.apsadv.2021.100069.
[60] M.B. Vukmirovic, N. Vasiljevic, N. Dimitrov, K. Sieradzki, Diffusion-limited current density of oxygen reduction on copper, J. Electrochem. Soc. 150 (2003), https://doi.org/10.1149/1.1526554. B10.
[61] F.C. Walsh, L.F. Arenas, G. Kear, The electrode kinetics of oxygen reduction: a case study. the corrosion of copper and its alloys in aqueous chloride solution at a smooth rotating disk electrode, Encycl. Interfacial Chem. Surf. Sci. Electrochem. (2018) 490–503, https://doi.org/10.1016/B978-0-12-409547-2.13771-0.
[62] A.D. Modestov, G.D. Zhou, Y.P. Wu, T. Notoya, D.P. Schweinsberg, A study of the electrochemical formation of Cu(I)-BTA films on copper electrodes and the mechanism of copper corrosion inhibition in aqueous chloride/benzotriazole solutions, Corros. Sci. 36 (1994) 1931–1946, https://doi.org/10.1016/0010-938X(94)90028-0.
[63] J. Crousier, L. Pardessus, J.P. Crousier, Voltammetry study of copper in chloride solution, Electrochim. Acta 33 (1988) 1039–1042, https://doi.org/10.1016/0013-4686(88)80192-0.
[64] M.R. Vogt, R.J. Nichols, O.M. Magnussen, R.J. Behm, Benzotriazole adsorption and inhibition of Cu(100) corrosion in HCl: a combined in situ STM and in situ FTIR spectroscopy study, J. Phys. Chem. B 102 (1998) 5859–5865, https://doi.org/10.1021/jp981216e.
[65] N. Elgrishi, K.J. Rountree, B.D. McCarthy, E.S. Rountree, T.T. Eisenhart, J. L. Dempsey, A Practical beginner's guide to cyclic voltammetry, J. Chem. Educ. 95 (2018) 197–206, https://doi.org/10.1021/acs.jchemed.7b00361.
[66] M. Finšgar, K. Xhanari, H.O. Ćurković, Cyclic voltammetry as an electroanalytical tool for analysing the reaction mechanisms of copper in chloride solution containing different azole compounds, Curr. Anal. Chem. 16 (2018) 465–474, https://doi.org/10.2174/1573411014666180704114202.
[67] M. Finšgar, EQCM and XPS analysis of 1,2,4-triazole and 3-amino-1,2,4-triazole as copper corrosion inhibitors in chloride solution, Corros. Sci. 77 (2013) 350–359, https://doi.org/10.1016/j.corsci.2013.08.026.
[68] M.C. Biesinger, L.W.M. Lau, A.R. Gerson, R.S.C. Smart, Resolving surface chemical states in XPS analysis of first row transition metals, oxides and hydroxides: Sc, Ti, V, Cu and Zn, Appl. Surf. Sci. 257 (2010) 887–898, https://doi.org/10.1016/j.apsusc.2010.07.086.
[69] P. Druska, H.H Strehblow, Quantitative determination of the passive layer on Cu–Ni alloys, Surf. Interface Anal 23 (1995) 440–450, https://doi.org/10.1002/sia.740230703.
[70] I. Milošev, H.H. Strehblow, Electrochemical behavior of Cu-xZn alloys in borate buffer solution at pH 9.2, J. Electrochem. Soc 150 (2003) B517, https://doi.org/10.1149/1.1615997.
[71] G. Deroubaix, P. Marcus, X-ray photoelectron spectroscopy analysis of copper and zinc oxides and sulphides, Surf. Interface Anal. 18 (1992) 39–46, https://doi.org/10.1002/sia.740180107.
[72] A.V. Naumkin, A. Kraut-Vass, S.W. Gaarenstroom, C.J. Powell, NIST X-ray photoelectron spectroscopy database, V4.1. (2012). 10.18434/T4T88K.
[73] P.M. Natishan, W.E. O'Grady, Chloride ion interactions with oxide-covered aluminum leading to pitting corrosion: a review, J. Electrochem. Soc. 161 (2014) C421, https://doi.org/10.1149/2.1011409jes.
[74] S.T. Pride, J.R. Scully, J.L. Hudson, Metastable pitting of aluminum and criteria for the transition to stable pit growth, J. Electrochem. Soc. 141 (1994) 3028, https://doi.org/10.1149/1.2059275.
[75] T. Hauffman, A. Hubin, H. Terryn, Study of the self-assembling of n-octylphosphonic acid layers on aluminum oxide from ethanolic solutions, Surf. Interface Anal. 45 (2013) 1435–1440, https://doi.org/10.1002/sia.5150.
[76] G. Viramontes-Gamboa, B.F. Rivera-Vasquez, D.G. Dixon, The active-passive behavior of chalcopyrite, J. Electrochem. Soc. 154 (2007) C299, https://doi.org/10.1149/1.2721782.
[77] E. Hoque, J.A. DeRose, P. Hoffmann, H.J. Mathieu, B. Bhushan, M. Cichomski, Phosphonate self-assembled monolayers on aluminum surfaces, J. Chem. Phys. 124 (2006), 174710, https://doi.org/10.1063/1.2186311.
[78] J. Torras, D.S. Azambuja, J.M. Wolf, C. Alemán, E. Armelin, How organophosphonic acid promotes silane deposition onto aluminum surface: a detailed investigation on adsorption mechanism, J. Phys. Chem. C 118 (2014) 17724–17736, https://doi.org/10.1021/jp5046707.
[79] C.D. Wagner, A.V. Naumkin, A. Kraut-Vass, J.W. Allison, C.J. Powell, J.R.J. Rumble, NIST standard reference databa se 20, Version 3.4 (web version), (2003). http://srdata.nist.gov/xps.
[80] M.R. Alexander, G.E. Thompson, G. Beamson, Characterization of the oxide/hydroxide surface of aluminum using X-ray photoelectron spectroscopy: a procedure for curve fitting the O 1 s core level, Surf. Interface Anal. 29 (2000) 468–477, https://doi.org/10.1002/1096-9918(200007)29:7%3C468::AID-SIA890%3E3.0.CO;2-V.
[81] M. Wagstaffe, A.G. Thomas, M.J. Jackman, M. Torres-Molina, K.L. Syres, K. Handrup, An experimental investigation of the adsorption of a phosphonic acid on the anatase TiO_2(101) surface, J. Phys. Chem. C. 120 (2016) 1693–1700, https://doi.org/10.1021/acs.jpcc.5b11258.
[82] J. Van den Brand, P.C. Snijders, W.G. Sloof, H. Terryn, J.H.W. De Wit, Acid-base characterization of aluminum oxide surfaces with XPS, J. Phys. Chem. B. 108 (2004) 6017–6024, https://doi.org/10.1021/jp037877f.
[83] A. Kokalj, D. Costa, Model study of penetration of Cl^- ions from solution into organic self-assembled-monolayer on metal substrate: trends and modeling aspects, J. Electrochem. Soc. 168 (2021), 071508, https://doi.org/10.1149/1945-7111/ac0a24.
[84] L. Zhang, J. Gao, L.N.W. Damoah, D.G. Robertson, Removal of iron from aluminum: a review, Miner. Process. Extr. Metall. Rev. 33 (2012) 99–157, https://doi.org/10.1080/08827508.2010.542211.